Frontiers in Bioscience Landmark

Front. Biosci. (Landmark Ed) **2025**; 30(4): 36415
https://doi.org/10.31083/FBL36415

Original Research

High-LET Proton Irradiation Significantly Alters the Clonogenic and Tumorigenic Potential of Human Breast Cancer Cell Lines *In Vitro* and *In Vivo*

Margarita Pustovalova[1,2,*], Rita Mohammad[1], Yuzhe Wang[1], Wenyu Xue[1], Philipp Malakhov[1], Viktor Nekrasov[1], Elizaveta Kontareva[1], Zain Nofal[1], Vyacheslav Saburov[3], Dmitry Kolesov[4,5], Andreyan Osipov[1,2], Sergey Leonov[1,6]

[1]Institute of Future Biophysics, 141701 Dolgoprudny, Russia
[2]State Research Center - Burnasyan Federal Medical Biophysical Center of Federal Medical Biological Agency, 123098 Moscow, Russia
[3]A. Tsyb Medical Radiological Research Center-Branch of the National Medical Research Radiological Center of the Ministry of Health of the Russian Federation, 249031 Obninsk, Russia
[4]Laboratory of Scanning Probe Microscopy, Moscow Polytechnic University, 107023 Moscow, Russia
[5]Institute of General Pathology and Pathophysiology, 125315 Moscow, Russia
[6]Institute of Cell Biophysics of Russian Academy of Sciences, 142290 Pushchino, Russia
*Correspondence: pustovalova.mv@mipt.ru (Margarita Pustovalova)
Academic Editor: Jordi Sastre-Serra
Submitted: 18 December 2024 Revised: 19 March 2025 Accepted: 3 April 2025 Published: 25 April 2025

Abstract

Background: The implementation of proton beam irradiation (PBI) for breast cancer (BC) treatment is rapidly advancing due to its enhanced target coverage and reduced toxicities to organs at risk. However, the effects of PBI can vary depending on the cell type. This study aimed to explore the effects of PBI on two BC cell lines, MCF7 and MDA-MB-231. **Methods**: The relative biological effectiveness (RBE) of PBI was assessed using a clonogenic assay. DNA double-strand break (DSB) repair, epithelial–mesenchymal transition (EMT), and filamentous actin (F-actin) were evaluated using immunofluorescence analysis. The extent of entosis and the senescence-associated β-galactosidase (SA-β-gal) activity were estimated by cytochemistry analysis. The influence of the extracellular matrix was evaluated by cultivating cells in both adherent two-dimensional (2D) environments and within 3D fibrin gels of varying stiffness. The metastatic propensity of cells was investigated using migration tests and the cell encapsulation of carboxylate-modified fluorescent nanoparticles. The comparative tumorigenic potential of cells was investigated using an *in vivo* model of the chick embryo chorioallantoic membrane (CAM). **Results**: PBI demonstrated superior efficacy in eliminating MCF7 and MDA-MB-231 cells with RBE 1.7 and 1.75, respectively. Following PBI, MDA-MB-231 cells exhibited significantly lower clonogenic survival compared to MCF7, which was accompanied by the accumulation of phosphorylated histone H2AX (γH2AX), p53-binding protein 1 (53BP1) and Rad51 foci of DNA DSBs repair proteins. After surviving 7 days post-PBI, MCF7 cells exhibited 2.5-fold higher levels of the senescence phenotype and entosis compared to the MDA-MB-231 offspring. Both PBI-survived cell lines had greater capability for 2D collective migration, but their metastatic potential was significantly reduced. A significant influence of extracellular matrix stiffness on the correlation between F-actin expression in PBI-survived cells—an indicator of cell stiffness—and their ability to uptake nanoparticles, a trait associated with metastatic potential, was observed. PBI-survived MDA-MB-231RP subline exhibited a hybrid EMT phenotype and a 70% reduction in tumor growth in the *in vivo* model of the chick embryo CAM. In contrast, PBI-survived MCF7RP cells exhibit mesenchymal-to-epithelial transition (MET)-like features, and their *in vivo* tumor growth increased by 66% compared to parental cells. **Conclusions**: PBI triggers various cellular responses in different BC cell lines, influencing tumor growth through mechanisms like DNA damage repair, stress-induced premature senescence (SIPS), and alterations in the stiffness of tumor cell membranes. Our insights into entosis and the effect of extracellular matrix stiffness on metastatic propensity (nanoparticle uptake) enhance the understanding of the role of PBI in BC cells, emphasizing the need for more research to optimize its therapeutic application.

Keywords: breast cancer; proton therapy; DNA damage repair; extracellular matrix (ECM) stiffness; stress-induced premature senescence (SIPS); entosis; stiffness of tumor cell membranes; mechanosensation; chick embryo chorioallantoic membrane (CAM) model

1. Introduction

Breast cancer is the most common cancer type among women worldwide and is the second leading cause of cancer-related deaths in this demographic globally [1]. Radiation therapy (RT) remains a cornerstone in the treatment of early [2] and metastatic [3] breast cancer (BC) as recommended by the European Society for Medical Oncology (ESMO) guideline committee. RT types are classified according to radiation quality measured by linear energy transfer (LET), which calculates energy deposited per unit length of a particle's path. Low-LET-based radiation (including X-rays, gamma radiation, and electrons) deposits lower amounts of energy per unit length and thus induces sparse and mostly single-strand DNA breaks (SSBs). Its usage in BC treatment can lead to cardiotoxicity, which is a significant side effect. The introduction of hadron therapy (high-LET), such as accelerated proton beams, offers significant advantages over conventional low-LET-based RT [4]. High-LET protons deposit higher concentrations of energy in a shorter distance when traversing tissue and induce highly localized clusters of DNA double-strand breaks (DSBs) [5]. Due to unique physical properties, proton beams enhance target coverage and enable the precise delivery of radiation doses. This improves cancer cell-killing efficacy while safeguarding healthy tissues and minimizing damage to organs at risk, such as the heart, lungs, and skin. Nevertheless, proton therapy (PT) presents certain challenges, notably its higher costs and limited accessibility compared to established photon irradiation techniques. Systematic reviews of clinical trials evaluating PT for BC indicate that it may not significantly improve overall treatment outcomes compared to photon therapy. However, these studies consistently report a substantial reduction in treatment-related toxicities, with radiation dermatitis being the most notable improvement [6,7]. Therefore, in clinical practice, it is crucial for radiation oncologists to meticulously evaluate patients before recommending PT to ensure that the dosimetric advantages translate into meaningful clinical outcomes [8].

Based on the expression of hormone receptors, i.e., the estrogen receptor (ER), progesterone receptor (PR), and human epidermal growth factor-2 (HER-2) receptors in the tumor, BC is classified into five subtypes: luminal types A and B, luminal B/Her-2+, triple negative/basal, and Her-2+ [9]. The triple-negative breast cancer (TNBC) subtype, characterized by negative ER, PR, and HER2 receptor status, poses a significant clinical challenge for oncologists due to its aggressive nature and the lack of effective therapies. Several authors have reported controversies with respect to the use of conventional RT for patients diagnosed with TNBC [10]. Since PT is an effective treatment for cancers located in hard-to-reach areas and those resistant to conventional radiotherapy, it is crucial to investigate whether PT can be a viable therapeutic option for TNBC.

In clinical practice, one of the most critical challenges is selecting individuals undergoing treatment with high- or low-LET radiation, based on the tumor's radiobiological properties which determine its radiosensitivity [11]. Analyzing differential gene expression profiles in primary and BC cell lines suggests that key factors influencing radiosensitivity include the activation of DNA repair pathways, the presence of cancer stem-like cells [5,12,13], hypoxia, and the complexity of the tumor microenvironment. To address this challenge effectively, it is essential to identify the precise molecular and phenotypic characteristics of tumor cells in response to RT. This deeper understanding will serve as the foundation for designing highly effective clinical treatment strategies. In the era of targeted therapies, recognizing biomarkers that define cancer cell responses is crucial for making informed therapeutic decisions. Transcriptional alterations specific to radiation types have been sporadically examined [14–17]. However, to our knowledge, there has been no systematic effort to characterize the molecular (at the protein level) and biological effects of high-LET radiation and radiation doses in BC cells with varying susceptibility to conventional low-LET RT. Establishing this knowledge base would be instrumental in differentiating the adverse side effects of high-LET RT from its beneficial cytotoxic and immunogenic properties.

In general, high LET radiation has a higher relative biological effectiveness (RBE). Recent study suggests a linear correlation between the doses of X-rays and protons required to achieve a specific fraction of surviving cells [18]. However, this relationship needs to be tested in specific BC cell lines. RBE varies depending on cell line-specific biological factors, such as their ability to repair DNA damage [19]. High-LET radiation typically induces a greater number of DSBs per dose unit and generates more complex, clustered lesions compared to low-LET radiation types [5]. This is due to its ability to deposit large amounts of energy over a short distance. Different forms of DNA damage activate distinct components of the DNA damage response (DDR) system, which plays a crucial role in repair. Several key DDR proteins are involved in this process and are commonly used to assess DNA damage. One of the most critical proteins modified near DNA damage sites is phosphorylated histone H2AX (γH2AX), which recruits repair proteins to the damaged site and initiates the repair process. γH2AX serves as a marker for DSBs, irrespective of the specific repair pathway employed by the cell. The DDR primarily operates through two major pathways: homologous recombination (HR) and classical non-homologous end joining (c-NHEJ). HR is a high-fidelity, template-dependent repair mechanism capable of handling complex DNA damage, including DNA gaps, DSBs, and interstrand crosslinks [20]. In contrast, NHEJ is an error-prone repair pathway in which DNA ends directly ligated by protein complexes [21]. Among the key proteins recruited to DNA damage sites is p53-binding protein 1 (53BP1), a

member of the Tudor-domain protein family [22]. In the G1 phase of the cell cycle, 53BP1 counteracts the function of breast cancer type 1 susceptibility protein (BRCA1)—an essential HR factor—by interacting with replication timing regulatory factor 1 (Rif1), thereby preventing 5′ end resection and promoting c-NHEJ [23,24]. During the S/G2 phases, BRCA1 and its partner CtIP inhibit Rif1 accumulation at DSB sites, thereby preventing 53BP1 interactions and favoring 5′-end resection, which directs repair toward HR or alternative end-joining (Alt-EJ) pathway [25]. Recent studies suggest that 53BP1 also regulates 5′-end resection, DSB mobility, and DSB integrity, preventing ectopic DSB recombination [26,27].Additionally, Rad51 is another key DSB-recruited protein that plays a crucial role in the HR-mediated repair pathway [28].

Cancer cell migration is essential for invasion and metastasis, as it involves changes in cell shape and rigidity to navigate through tight tissue spaces [29]. During this process, cells often acquire increased invasiveness and resistance to anoikis, a form of programmed cell death [30]. Research on resistance mechanisms has not clearly explained how migration in confined spaces relates to the development of therapeutic resistance.

Research shows that irradiation can change tumor aggression by either reducing or increasing the invasiveness of surviving cancer cells, which depends on the cell line and type of radiation [31]. However, the effects of proton irradiation on the characteristics of tumor cells that survive and migrate through porous tumor tissue have not been fully studied. Understanding these changes is essential for developing effective treatments that target the migratory and invasive capabilities of cancer cells. Proton irradiation may inhibit cellular migration, as studies show it reduces cell motility in melanoma cells and alters the expression of migration and adhesion proteins [32,33]. However, the impact of proton irradiation on cancer cell migration and resistance, especially in TNBC, needs more research to uncover its therapeutic potential.

In this study, we aimed to assess the differential biological effects of high- and low-LET radiation doses on the clonogenic survival rates of MCF7 and MDA-MB-231 cell lines, widely used *in vitro* models representing ER-positive and TNBC/Claudin-low breast tumors, respectively. These models exhibit distinct metastatic phenotypes and varying degrees of susceptibility to conventional low-LET RT [34]. As a key component of the BC cell survival response, the molecular reaction to DNA DSBs was evaluated through quantitative high-content immunofluorescence analysis of radiation-induced foci (RIF) of γH2AX, 53BP1, and Rad51 proteins following 2 Gy of proton beam irradiation (PBI). Additionally, we conducted an in-depth analysis of MCF7 and MDA-MB-231 populations, that survived a single lethal dose (6 Gy) of PBI. These surviving sublines, designated as MCF7RP and MDA-MB-231RP, were further investigated to characterize their molecular and phenotypic traits, particularly those associated with growth and metastatic potential, in both *in vitro* and *in vivo* settings.

2. Materials and Methods

2.1 Cell Lines and Culture Conditions

BC cell lines, MDA-MB-231 and MCF7 were sourced from ATCC (Manassas, VA, USA). MDA-MB-231 cells are characterized by their triple-negative status (ER-/PR-/HER2-) and TP53 deficiency, while MCF7 cells are estrogen receptor-positive (ER+) and progesterone receptor-positive (PR+), with intact TP53 function. Both cell lines were cultured in DMEM medium (PanEko, Moscow, Russia) containing 4.5 g/L glucose and 1% L-glutamine, supplemented with 10% fetal bovine serum (FBS), 100 U/mL penicillin, 100 U/mL streptomycin, and sodium pyruvate (PanEko, Moscow, Russia). The cells were maintained at 37 °C in a humidified atmosphere with 5% CO_2. Cell line authenticity was verified through STR profiling, and they tested negative for mycoplasma contamination using the MycoReport Mycoplasma Detection Kit (Cat. # MR001, Evrogene, Russia).

2.2 Proton Beam Irradiation

Cells were irradiated at the Russian Proton Accelerator “Prometheus” of A. Tsyb Medical Radiological Research Centre (MRRC, Obninsk, Russia). Irradiation was carried out at the middle spread-out Bragg peak (SOBP, 15 mm width), with doses of 2, 4, and 6 Gy, with 70 $\times$ 83 mm^2 field size (energy range 94.40–105.30 MeV, LET 5.2 kEv/µm). Cell culture flasks were positioned upright and irradiated by directing the collimated beam at the flask surface. To ensure uniform exposure, the flasks were covered by delivering multiple shots that collectively encompassed the entire surface area. Flasks were placed on a piece of special plastic equipment at a reference depth in the center of the field with the help of laser centralizers. To ensure accurate radiation delivery, depth dose profiles were determined, and dosimetric calibrations were conducted using a water phantom PTW MP3-P Water tank using a plane-parallel ionization chamber Advanced Markus Chamber Type 34045 (SE 002617) (PTW, Freiburg im Breisgau, Germany). The dosimetric system was calibrated under reference conditions [35]. For γ-irradiation, the Rokus-AM facility (Rawenstvo, Russia) was used (Co^{60} source, dose-rate 0.613 Gy/min^{-1}).

2.3 Clonogenic Assay

Cells were seeded in T25 tissue culture flasks 24 h prior to irradiation at 3–5 $\times$ 10^5 cells per flask. After irradiation, cells were seeded on 6-well plates at opportune densities (100, 500, 1000, and 2000 cells/well for doses of 0, 2, 4, and 6 Gy, respectively) according to the dose delivered to assay. Untreated cells served as a control to assess the plating efficiency (PE). Cells were cultured under standard

conditions for 14 days, forming colonies. They were then fixed with methanol and stained with Giemsa. Colonies containing more than 50 cells were manually counted using a Zeiss Axiovert microscope with phase-contrast capabilities (Carl Zeiss, Göttingen, Germany). Dose–response data were generated from the mean of three independent experiments. Each biological repeat contained at least three replicates.

PE and survival fraction (SF) were subsequently calculated using the formula:

$$PE = \frac{\text{number of colonies}}{\text{number of cells seeded in a well}} \times 100\% \quad (1)$$

$$SF = \frac{\text{number of colonies formed after irradiation}}{(\text{ number of cells seeded } \times PE)} \quad (2)$$

2.4 Calculation of Relative Biological Effectiveness

RBE is defined as the ratio of the absorbed dose of the reference radiation (gamma-irradiation, Co^{60}, Dref) to the absorbed dose of the test radiation (proton Beam, D) required to achieve the same biological effect (Eqn. 3).

$$RBE = \frac{\text{Dref}}{D} \quad (3)$$

The biological endpoint is assessed through *in vitro* clonogenic survival, which is typically modeled using the linear quadratic model (LQM).

$$S = \exp\left(-\alpha D - \beta D^2\right) \quad (4)$$

where the surviving fraction S as a function of the absorbed dose D, α and β are exposure- and cell-specific fitting parameters.

Thus, the RBE was evaluated as a function of the surviving fraction S (RBES) using Eqn. 5:

$$RBES = \frac{\alpha + \sqrt{\alpha^2 - 4\beta ln(S)}}{\alpha ref + \sqrt{\alpha^2 ref - 4\beta ref ln(S)}} \quad (5)$$

where α, β, αref, and βref are the linear and quadratic terms of the LQM for the radiation under investigation and the reference photon exposure, respectively.

2.5 Immunofluorescent Analysis for γH2AX, 53BP1, and Rad51 Foci

Prior to irradiation, cells were seeded at a density of 0.1×10^5 cells/0.32 cm^2 in 96-well plates. Cells were exposed to 2 Gy PBI (10 mm modified Bragg peak, 90 × 130 mm^2 field size, energy range 96.00–103.15 MeV).

Following incubation for 1, 12, 24, and 48 hours, cells were fixed in 4% paraformaldehyde in PBS (pH 7.4) for 20 minutes at room temperature. After two PBS rinses, cells were permeabilized with 0.3% Triton-X100 (PanEko, Moscow, Russia) in PBS supplemented with 2% BSA to prevent nonspecific antibody binding. Cells were then incubated with primary antibodies against γH2AX (dilution 1:200, clone JBW301, MerckMillipore, Burlington, VT, USA), Rad51 (1:200 dilution, Cat. # ABE257, Merck Millipore, Burlington, VT, USA), and 53BP1 (1:200 dilution, Cat. # MAB3802, Merck-Millipore, Burlington, VT, USA) for 1 hour at room temperature. The primary antibodies were diluted in PBS with 1% BSA. Following three PBS washes, cells were incubated with secondary antibodies conjugated to Alexa Fluor 488 (1:800 dilution; Cat. #A-21424, Merck-Millipore, Burlington, VT, USA) and Cy3 (1:500 dilution; Cat. #AP124C, Merck Millipore, Burlington, VT, USA) for 1 hour. Nuclei were stained with Hoechst 33342 (Thermo Fisher Scientific, Waltham, MA, USA). Images were captured using a JuLI Stage automatic cell analyzer (NanoEntek, Seoul, Korea) with a 40× objective. Foci were manually counted, and data were derived from the mean of three independent experiments, each containing two replicates, with at least 100 cells analyzed per sample.

2.6 Analysis of Senescence-Associated β-Galactosidase-Positive Cells

The proportion of cells expressing senescence-associated β-galactosidase (SA-βgal) was determined using a commercial Cellular Senescence Assay kit (EMD Millipore, Burlington, VT , USA, Cat. # KAA002). Cells were stained according to the manufacturer's instructions, and nuclei were counterstained with Hoechst 33342. Visualization was performed using the EVOS FL Auto Imaging System (Fisher Scientific, Pittsburgh, PA, USA) with a 20× objective lens. The percentage of SA-βgal-positive cells, along with entotic cells, was manually calculated from three independent experiments, each containing three replicates, with at least 200 cells analyzed per sample. Statistical analysis was conducted using the Kruskal–Wallis test via GraphPad Prism software 9.0.2.161 (GraphPad Software, San Diego, CA, USA).

2.7 Growing 3D Spheroids in Fibrin Gel

Cells were seeded in 3D fibrin gel using the protocol described previously [36]. Fibrin gels were fabricated using human fibrinogen and thrombin (NPO RENAM, Moscow, Russia). The fibrinogen powder was dissolved in sterile 0.9% saline solution at 37 °C to get 20 mg/mL concentration, aliquoted and stored at –80 °C. Thrombin stock (0.1 U/µL) was prepared by dissolving 1000 U thrombin powder in 10 mL T7 buffer (50 mM Tris, 150 mM NaCl, pH 7.4) and stored at –80 °C in 150 µL aliquots. Gel of 90 and 1050 stiffness was prepared according to Table 1.

Table 1. Fibrin gel stiffness is controlled by varying amounts of fibrinogen.

Gel stiffness (Pa)	Fibrinogen (µL)	T7 buffer (µL)	Cells mixture/culture medium (µL)	Thrombin (µL)	Total (µL)
90	12.5	112.5	125	5	255
1050	100	25	125	5	255

For live 3D colony growth monitoring, 5000 MCF7 cells and 8000 MDA-MB-231 cells were seeded into 3D fibrin gels per well in a 24-well plate. Two wells were made for each condition and at least 20 images of colonies were captured in each well every two days on an EVOS M5000 fluorescent microscope (Thermo Fisher Scientific, Waltham, MA, USA) in a transmitted light channel with a 20× objective. The colony sizes were quantitatively estimated from digital images using the ImageJ software IJ 1.46r (Laboratory for Optical and Computational Instrumentation, University of Wisconsin, Madison, WI, USA).

2.8 Immunofluorescence Analysis of Epithelial–Mesenchymal Transition (EMT) Markers and F-Actin

Cells were seeded in 384-well plates at a concentration of 2.5×10^3 cells/well. On the next day, cells were fixed with 4% paraformaldehyde for 15 min and rinsed three times with 1× PBS (pH 7.4). After blocking and permeabilization with 2% BSA and 0.3% Triton in 1× PBS (pH 7.4) for 45 min at room temperature, cells were incubated with primary antibodies against E-Cadherin (1:400 dilution, Cat. # ab40772, Abcam, Cambridge, UK), N-Cadherin (1:400 dilution, Cat. # ab76011, Abcam, Cambridge, UK), Vimentin (1:500 dilution, Cat. # ab92547, Abcam, Cambridge, UK), and SNAIL (1:500 dilution, Cat. # ab85936, Abcam, Cambridge, UK) diluted in 1× PBS with 2% BSA and 0.3% Triton X100, overnight at +4 °C. Goat anti-rabbit IgG Alexa Fluor 488 (1:1000 dilution, Cat. # ab150077, Abcam, Cambridge, UK) was used as a secondary antibody (2 µg/mL) for 3 hours at room temperature. Nuclei were counterstained with Hoechst 33342 (6 µg/mL, Thermo Scientific, Rockford, IL, USA).

To prepare the cells for analysis of filamentous actin (F-actin), they were fixed using a solution containing 4% paraformaldehyde diluted in 1× PBS for a period of 15 minutes. Following this fixation step, the cells were permeabilized with 0.2% Triton X-100, allowing for a consistent permeabilization process that lasted for 20 minutes. The cells were subsequently blocked using a 2% solution of BSA in 1× PBS (PBS-2%BSA) for one hour at room temperature. Following this, F-actin staining was performed using the Phalloidin-iFluor 488 Reagent (Abcam, Cat. # ab176753, Cambridge, UK) in PBS, adhering to the manufacturer's protocol. Cells were imaged using the EVOS M5000 fluorescent microscope with a 20× objective. The results were obtained from three independent experiments with three replicates.

2.9 "Scratch" (Wound Healing) Test

Non-irradiated and irradiation-survived MCF7 and MDA-MB-231 cells were seeded at a density of 5×10^5 cells per well in a 6-well plate. The cells were cultured in a humidified atmosphere with 5% CO_2 at 37 °C to form a confluent monolayer. After 24 hours in depleted medium (1% FBS), the cell monolayer was wounded using a sterile micropipette tip, creating a straight line scratch. The monolayer was then washed with PBS to remove cellular debris. The initial and final wound areas were imaged at 0 and 24 hours post-wounding using an EVOS M5000 microscope with a 10× objective. Wound healing was quantified as a percentage using the Eqn. 6:

$$\text{Wound healing, \%} = ((\text{WA0 h}) - (\text{WA}\Delta\text{ h})) / (\text{WA0 h}) \times 100\% \quad (6)$$

where WA0 h is the initial wound area, measured immediately after creating the wound, and WAΔ h is the area after 24 hours. The percentage of wound healing was calculated as the mean with standard error of the mean (SEM) from two independent experiments, each with three replicates. Statistical analysis was performed using the Kruskal–Wallis test via GraphPad Prism software to compare the healing rates of parental and irradiated cells.

2.10 Nano-Bead Endocytosis Test

The test was performed according to our previously published protocol [37]. Briefly, carboxylate-modified fluorescent 200 nm in diameter particles (excitation/emission 505/515 nm) (Invitrogen life technologies, Carlsbad, CA, USA) were used to evaluate the adhesion and encapsulation efficiency of the cells. Cells were seeded in 96-well plates (Corning Incorporated, Corning, NY, USA) at a concentration of 5000 cells per well. Nanoparticles (NPs) were added to the cells to achieve the final concentration of approximately 2000 particles per cell. Nuclei were stained with Hoechst 33342. Cells were incubated for 1 hour at 37 °C, then washed with PBS and treated with trypsin to remove non-internalized particles. Cell viability was confirmed using a live/dead nuclei fluorescent stain. Negative controls, consisting of cells without nanoparticles, were also evaluated under the same conditions. Data were obtained from 3 independent experiments, each sample contained at least 3 replicates.

2.11 Trans-Well Migration Assay Using Boyden Chambers

For the analysis of cell migration through physically confined environments cells were serum-starved overnight and then seeded in the upper compartment of Transwell inserts (Cat.# 3428 , EDM Milli-pore, Billerica, MA, USA) containing 0.1 mL of serum-free medium specific to the cell type. The inserts had 8 µm pores and were placed in wells with serum-supplemented growth medium in the lower chamber, which served as a chemoattractant. Cells were incubated for 72 hours at 37 °C and 5% CO_2. Following incubation, cells from both compartments were collected by trypsinization and counted using a hemocytometer after neutralization with a serum-containing medium. For each cell type, the experiment was repeated 6 to 9 times, with three replicates per experiment, to determine the percentage of cancer cells that migrated through the membrane.

2.12 Scanning Ion-Conductance Microscopy Measurements of Cell Stiffness

Scanning ion-conductance microscopy (SICM) was employed to evaluate the mechanical stiffness of cell membranes. This advanced technique utilizes a nanoscale glass capillary filled with an electrolyte solution, which performs hopping movements to effectively map the topographical and mechanical properties of biological samples adhered to a substrate also immersed in the same solution.

The measurement of ion current occurs through the capillary tip, which is positioned between two AgCl electrodes that are submerged in the electrolyte solution, both inside and outside the capillary probe. This configuration allows for precise control over the interaction between the probe and the sample surface. For topographical mapping, a setpoint for an ion current decrease of 0.4% was utilized, while 1% and 2% were applied to assess stiffness. The Young's modulus was subsequently calculated using the methodology established by Rheinlaender and Schäffer [38].

The SICM measurements were conducted using an instrument from ICAPPIC Ltd. (Moscow, Russia), which was equipped with a 1.2 mm borosilicate glass capillary that had been shaped using a P-2000 laser puller (Sutter Instrument, Novato, CA, USA). The inner diameter of the capillary tip was approximately 50 nm, as determined by measuring the ion current in a buffer solution.

For these SICM assessments, cells were seeded at a density of 100,000 cells per 35 mm Petri dish and incubated overnight at 37 °C in a CO_2 incubator. Prior to conducting measurements, the culture medium was replaced with an HBSS buffer solution that served as the electrolyte.

2.13 CAM (In Vivo) Assay

Fertilized specific pathogen-free (SPF) eggs were purchased from a local SPF hatchery. The surface of the eggs was cleaned with paper towels and sterile water, and then placed horizontally in an incubator set to 37 °C and 70% relative humidity, with the automatic rotation function activated. This day was designated as embryonic day 0 (EMD 0). On embryonic day 3 (EMD 3), the eggs were removed, and the air sacs and major blood vessels were identified and marked using an egg candler. Approximately 3 mL of egg white was then withdrawn, and upon observing the chorioallantoic membrane (CAM) drop, a 2 cm diameter circle was drawn at the drop location. The eggshell was cut along the marked edges using a mini chainsaw, and the window was sealed with 3M semipermeable film before the eggs were returned to the incubator, with the automatic rotation function turned off. On EMD 9, tumor cells were seeded. The eggs were removed, the semipermeable membrane was peeled off, and an O-ring (polytetrafluoroethylene (PTFE) O-ring, with an inner diameter of 6 mm and an outer diameter of 9 mm) was placed over the window near the densely vascularized area of the CAM. Twenty-five µL of a serum-free cell suspension containing 5×10^6 cells was injected into the ring, after which the window was resealed with the semipermeable membrane, and the eggs were returned to the incubator. Eggs were collected on EMD 16, and tumors were imaged using a Leica M60 microscope (Leica Microsystems, Singapore, Republic of Singapore). To evaluate tumor growth characteristics, image analysis was performed using the ImageJ software. To account for potential variations in camera height during imaging, which could introduce discrepancies in absolute area measurements, the inner ring region with known size was used as a reference. This approach minimizes size deviations, enhancing the accuracy and comparability of the data. Additionally, the mean grayscale value of the target region was measured, where grayscale intensity in digital images, which reflects the optical density or thickness, serves as an approximate indicator of tumor tissue density or thickness in this study. The tumor size was estimated by calculating the ratio of the tumor area to the outer ring area, which was then multiplied by the normalized grayscale value, represented on the graph in arbitrary units (a.u.). Data were obtained from 3 individual tumors per sample.

The CAM xenograft experiments in this study were conducted in strict compliance with the guidelines and regulations of the Institutional Animal Care and Use Committee (IACUC). Chicken embryos are not classified as living animals until 17 days of incubation [39,40], and our experiments with CAM were completed by embryonic day 16 (E16), which were exempt from IACUC regulation. Additionally, in adherence to the Russian Animal Experiment and Welfare Guidelines, ethical approval was not required. Daily assessments were carried out to ensure embryonic viability.

2.14 Statistical Analysis

Statistical analysis was performed using Student's *t*-test, the Mann–Whitney U-test, and two-way ANOVA with

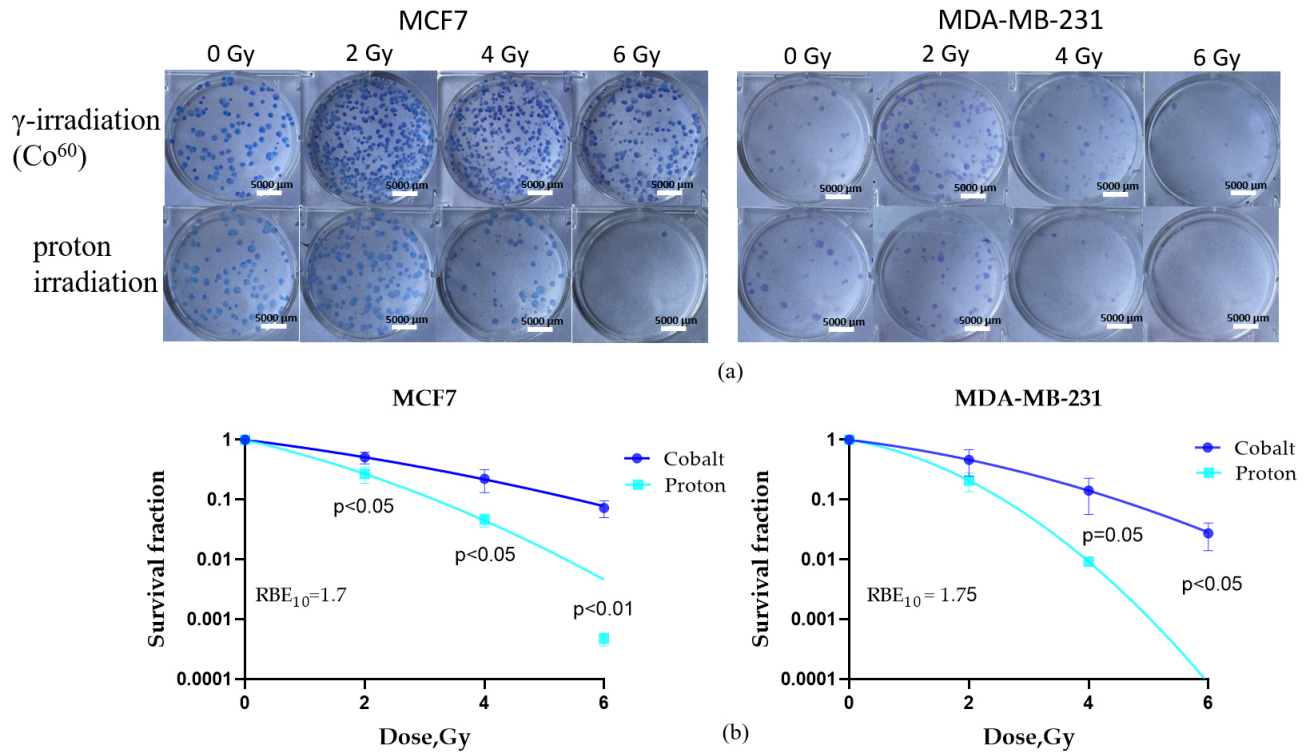

Fig. 1. Cell survival clonogenic assay was performed to evaluate the RBE of proton beam irradiation. Representative pictures of colonies grown after each irradiation dose of gamma and proton beam irradiation of MCF7 and MDA-MB-231 (a) cells. Survival curves of MCF7 and MDA-MB-231 (b) cell lines after proton and gamma (Co^{60} source) irradiation at doses of 2, 4, and 6 Gy were calculated. Data are means ± SD of three independent experiments. Statistical significance between groups indicated on the graphs was calculated with Student's *t*-test. Scale bar 5000 µm. RBE, relative biological effectiveness.

Tukey's post-hoc test for multiple comparisons, all facilitated by GraphPad Prism 8 software. Results are presented as means ± standard deviation (SD) from three independent experiments unless otherwise specified. Significance levels were indicated by asterisks: * for $p < 0.05$, ** for $p \leq 0.01$, *** for $p \leq 0.001$, and **** for $p \leq 0.0001$.

3. Results

3.1 Assessment of RBE After Proton Beam Irradiation of Breast Cancer Cell Lines

In this study, we first investigated the RBE of PBI for two BC cell lines, MCF7 and MDA-MB-231 (Fig. 1a), using clonogenic assay. Our goal was to examine the unique interplay between biological factors influencing physical parameters controlling the LET effect and innate radiosensitivity in determining a cell's reaction to protons.

RBE is a fundamental concept in radiation biology that quantifies the effectiveness of different types of ionizing radiation in inducing biological effects, typically in comparison to standard reference radiation, such as X-rays or gamma rays [41]. Using gamma irradiation from the Co^{60} source as a reference, RBE was calculated based on the linear quadratic model (LQM), the most widely used model for predicting cell survival in radiation therapy. Following PBI, the radiosensitivity of MCF7 cells, as indicated by survival fraction, significantly decreased compared to gamma irradiation ($p < 0.05$ for 2, 4, and 6 Gy) (Fig. 1b). In MDA-MB-231 cells, proton irradiation resulted in an even more pronounced reduction in radiosensitivity. However, statistical significance was only reached at 6 Gy compared to gamma irradiation ($p < 0.05$) (Fig. 1b). The RBE of PBI at 10% cell survival fraction (i.e., SF = 0.1) was found to be 1.7 for MCF7 cells and 1.75 for MDA-MB-231 cells, confirming the superior efficacy of PBI in eliminating cancer cells compared to gamma irradiation. Notably, MDA-MB-231 cells exhibited the lowest clonogenic survival rates following high-LET irradiation, indicating a heightened sensitivity to protons compared to MCF7 cells.

After a continuous cultivation period of 3 to 4 weeks in T-25 tissue culture flasks, we observed that a distinct subset of cells that survived high-LET radiation from each parental cell line successfully generated viable progeny. These progeny were designated as the MDA-MB-231RP and MCF7RP sublines for further investigation (see follow-up Sections 3.4–3.8). All subsequent experiments involving irradiation-survived progeny were conducted within 10 passages.

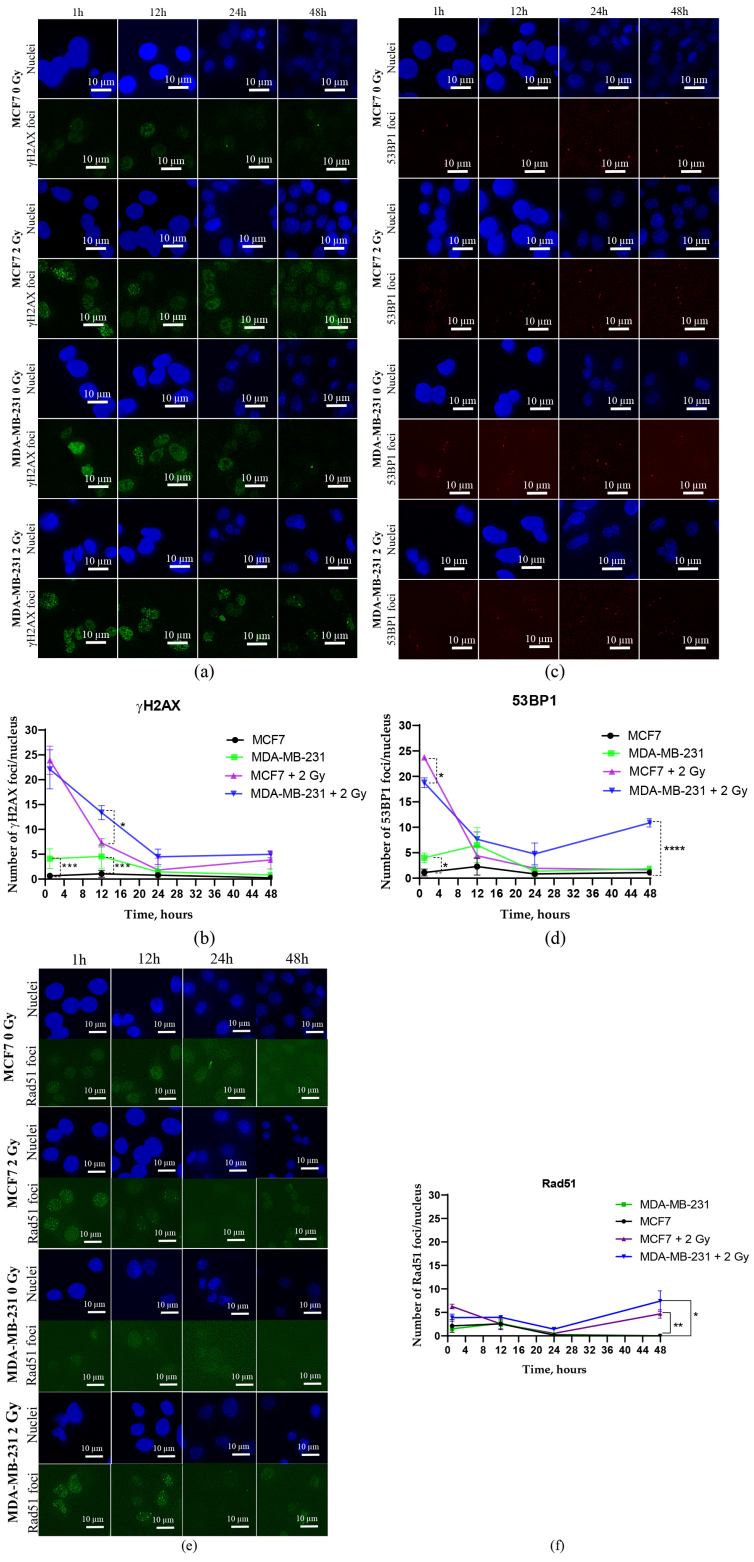

Fig. 2. Immunofluorescence images and quantitative immunofluorescence data illustrating the kinetics of DNA DSBs repair proteins. Quantitative immunofluorescence analysis was performed to calculate the kinetics of RIF numbers of key DDR proteins, namely γH2AX (a), 53BP1 (c), and Rad51 (e). Kinetics of changes in the number of γH2AX (b), 53BP1 (d), and Rad51 (f) foci in the cell's nucleus after 2 Gy of proton beam irradiation. Statistical significance calculated by Student's *t*-test. * $p < 0.05$, ** $p \leq 0.01$, *** $p \leq 0.001$, **** $p \leq 0.0001$. Data are means ± SEM of three independent experiments. Scale bar 10 μm. RIF, radiation-induced foci; DDR, DNA damage response; γH2AX, phosphorylated histone H2AX; 53BP1, p53-binding protein 1; SEM, standard error of the mean.

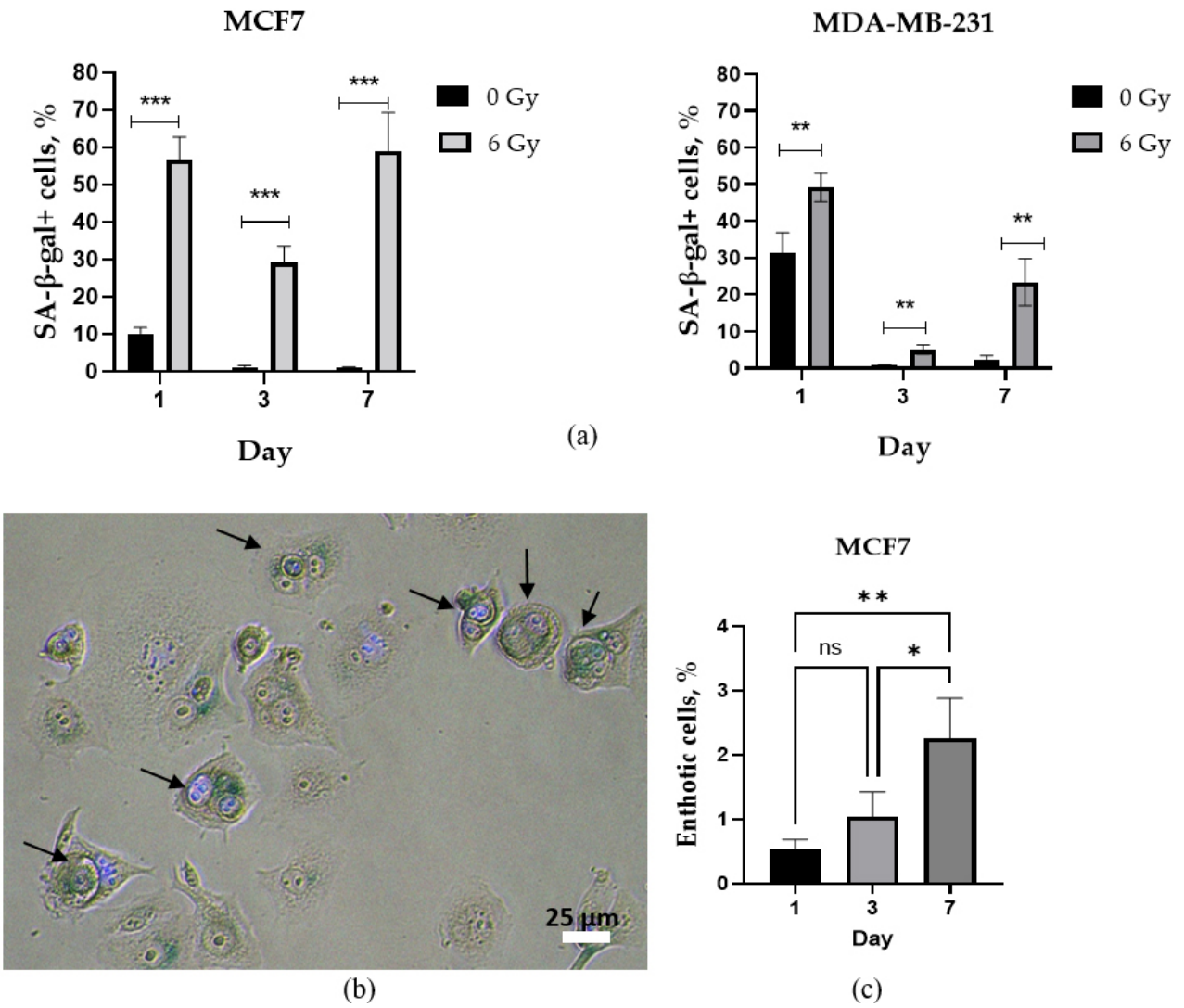

Fig. 3. Quantitative analysis of senescence-associated β-galactosidase (SA-β-gal) staining. The proportion of the senescent cells in MCF7 and MDA-MB-231 (a) populations after proton beam irradiation. Representative image of entotic cells in MCF7 irradiated by 6 Gy of proton beam (indicated by black arrows) (b). Cytoplasm of β-galactosidase positive cells stained in green. Nuclei (blue) stained by Hoechst 33342. Changes in the proportion of entotic cells in proton irradiation-survived (RP) MCF7 population by day 1, 3, and 7 (c). Statistical significance calculated by Student's *t*-test. * $p < 0.05$, ** $p \leq 0.01$, *** $p \leq 0.001$, ns, not significant. Data are means $\pm$ SEM from three independent experiments. Scale bar 25 µm.

3.2 Molecular Response to Altered DNA Sequences After Proton Beam Irradiation of MCF7 and MDA-MB-231 Cell Lines

After radiation exposure, DNA damage response (DDR) proteins are rapidly recruited and/or modified at DSB sites leading to their accumulation at the damage site. This results in the formation of nuclear foci, known as radiation-induced foci (RIF), which are detectable under fluorescent microscopy. RIF quantification serves as an indirect method for assessing DNA damage and repair by monitoring the molecular response to DNA alterations, ultimately reflecting the resolution of RIF. Typically, RIF measurements are performed on fixed samples at defined time points following ionizing radiation (IR) exposure [42].

Our observed differences in the sensitivity of TNBC (MDA-MB-231) and ER-positive (MCF7) cell lines to PT (Fig. 1) raised important questions regarding the DDR protein signatures associated with cell sensitivity to high- versus low-LET radiation. We further aimed to explore the molecular mechanisms underlying the heightened biological impact of protons, as well as potential proton-specific resistance mechanisms. Using quantitative immunofluorescence analysis, we calculated the kinetics of RIF formation for key DDR proteins, γH2AX (Fig. 2a), 53BP1 (Fig. 2c), and Rad51 (Fig. 2e) in BC cell lines following 2 Gy PBI. At 1 hour post-irradiation, the number of γH2AX RIF in MCF7 and MDA-MB-231 cells was nearly identical (Fig. 2b). However, extending the incubation period to 12

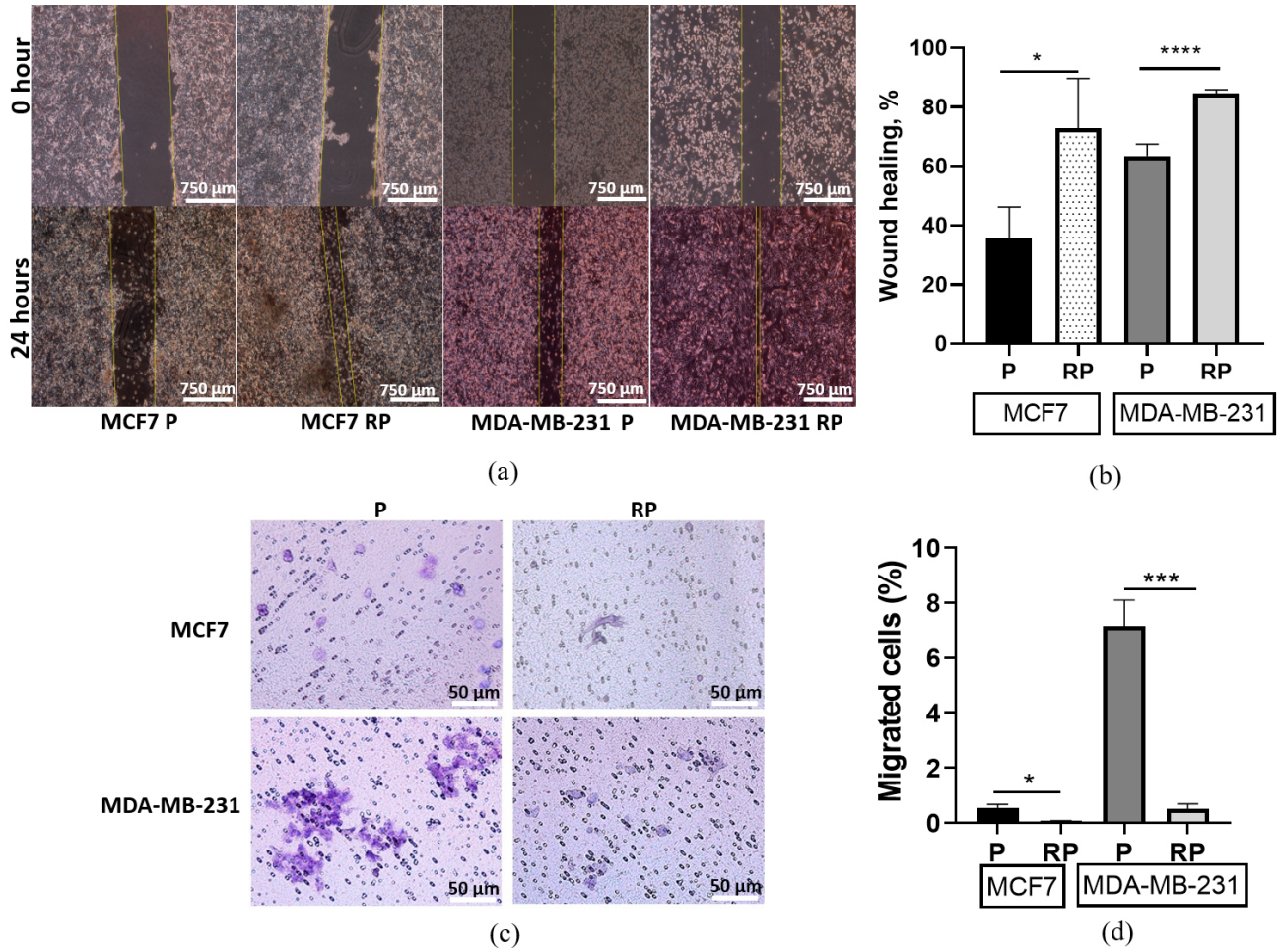

Fig. 4. Collective (wound healing assay) and confined (through 8 µm pores of Boyden chamber membranes) migration of parental (P) and proton irradiation-survived (RP) MCF7 and MDA-MB-231 cell lines. Representative images at 24 hours after wound formation (a). Scale bar 750 µm. Bar-graphs of changes in wound healing percentage (b). Representative pictures of Giemsa-stained cells on the outer surface of the Boyden chamber membranes at 48 hours of confined migration (c). Scale bar 50 µm. Bar graphs of the fraction of cells migrated into the lower Boyden chamber (d). Data are means of three replicates ± SD. Scale bar 50 µm. Statistical significance calculated by Student's *t*-test. * $p < 0.05$; *** $p \leq 0.001$; **** $p \leq 0.0001$. SD, standard deviation.

hours revealed significant differences between the two cell lines. MDA-MB-231 cells exhibited approximately twice as many γH2AX RIF per nucleus compared to MCF7 cells ($p < 0.05$). Furthermore, in MCF7 cells, γH2AX RIF numbers did not return to baseline even after 48 hours of incubation. Notably, non-irradiated MDA-MB-231 cells displayed a higher intrinsic level of spontaneous γH2AX foci at both 1 hour and 12 hours post-treatment compared to MCF7 cells (Fig. 2b).

MCF7 cells exhibited a significantly higher number of 53BP1 RIF at the initial time point (1 hour) post-irradiation compared to MDA-MB-231 cells ($p < 0.05$) (Fig. 2d). In MCF7 cells, this key marker of the NHEJ pathway for DNA DSB repair was resolved within approximately 12 hours, returning to baseline levels. In contrast, MDA-MB-231 cells displayed a different repair kinetics pattern. At 12 hours post-irradiation, the number of 53BP1 RIF had decreased to only 50% of the levels observed at 1 hour. Strikingly, by 48 hours post-irradiation, the number of 53BP1 RIF in irradiated MDA-MB-231 cells increased rather than resolving. Additionally, in non-irradiated MDA-MB-231 cells, 53BP1 foci remained consistently high throughout the 1–12 hour period (Fig. 2d).

In irradiated MCF7 cells, the initial peak of Rad51 RIF, a key marker of the homologous recombination (HR) pathway, reached approximately 5 foci per nucleus (Fig. 2e) and gradually declined to baseline levels by 24 hours (Fig. 2f). Increasing the incubation time to 48 hours resulted in more Rad51 RIF in both irradiated cell lines. In irradiated MDA-MB-231 cells, the number of Rad51 RIF remained above control levels at all examined time points (Fig. 2f). Notably, at 48 hours post-irradiation, Rad51 RIF levels were significantly higher compared to control levels ($p < 0.01$).

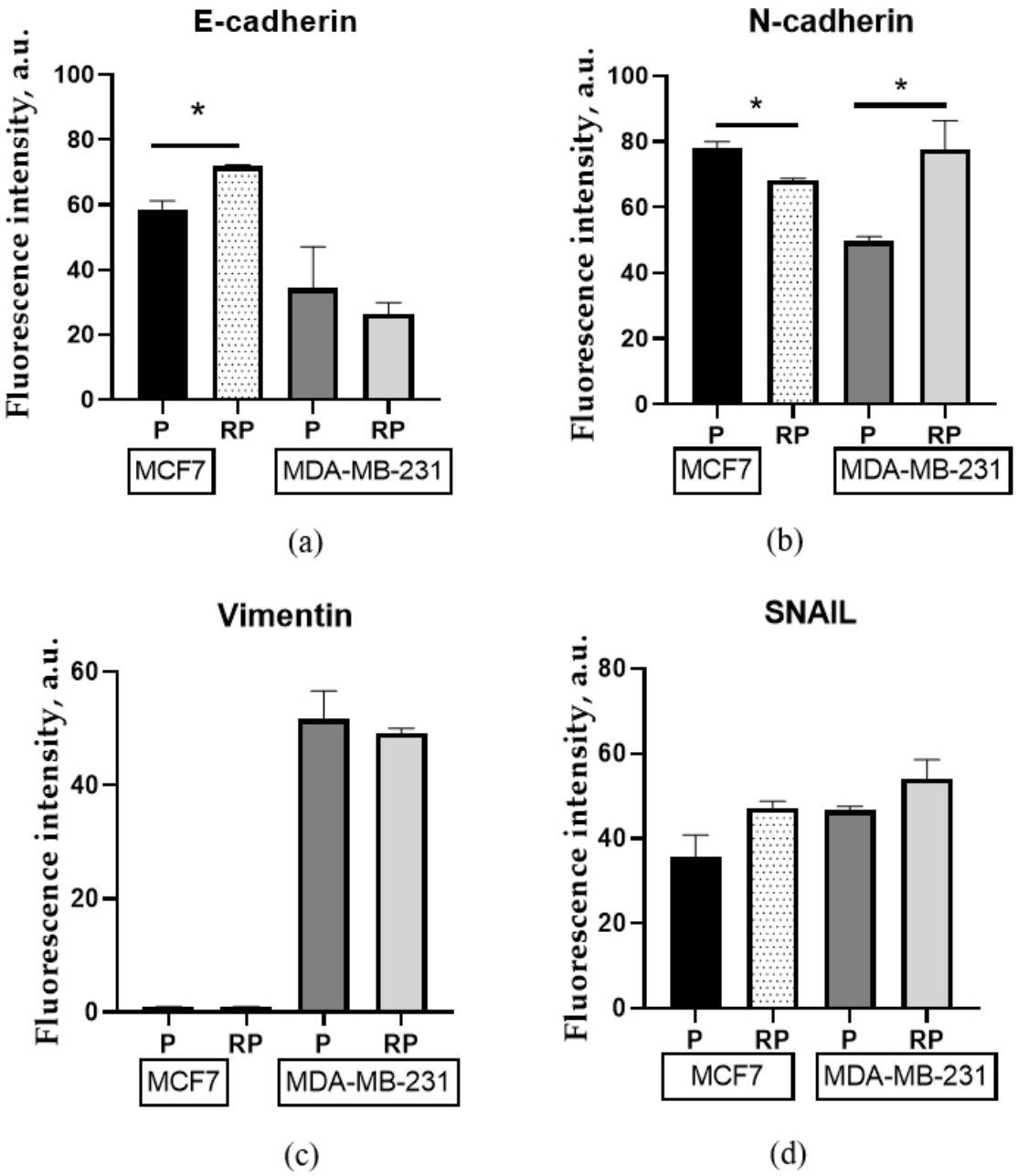

Fig. 5. Analysis of EMT marker expression in parental (P) and proton irradiation-survived (RP) MCF7 and MDA-MB-231 cells. The expression changes of E-cadherin (a), N-cadherin (b), Vimentin (c), and SNAIL (d) were analyzed using high-content immunofluorescent imaging and analysis. Statistical significance calculated by Student's *t*-test. * $p < 0.05$. Data are means ± SD from three independent experiments.

3.3 Analysis of High-LET-Induced Premature Senescence and Entosis

The emergence of IR-induced cell senescence, a form of stress-induced premature senescence (SIPS) [43], represents a potential method to assist cancer cells in overcoming RT, and it may exacerbate the biological behavior of tumor cells after IR treatment [44]. Therefore, we sought to determine whether SIPS also contributes to the differences in radiosensitivity and DDR network functionality induced by high-LET radiation between MCF7 and MDA-MB-231 cells. Specifically, we aimed to investigate whether SIPS is associated with the inaccurate repair of DNA damage following high-LET irradiation.

To address this, we analyzed the proportion of senescent cells on days 1, 3, and 7 post-irradiation using analysis of the senescence-associated (SA) β-galactosidase (SA-β-gal). β-galactosidase is a lysosomal hydrolase, which accumulates in the cytoplasm of senescent cells giving green-blue staining at pH = 6 during analysis [45]. In non-irradiated cells, the fraction of β-galactosidase posi-

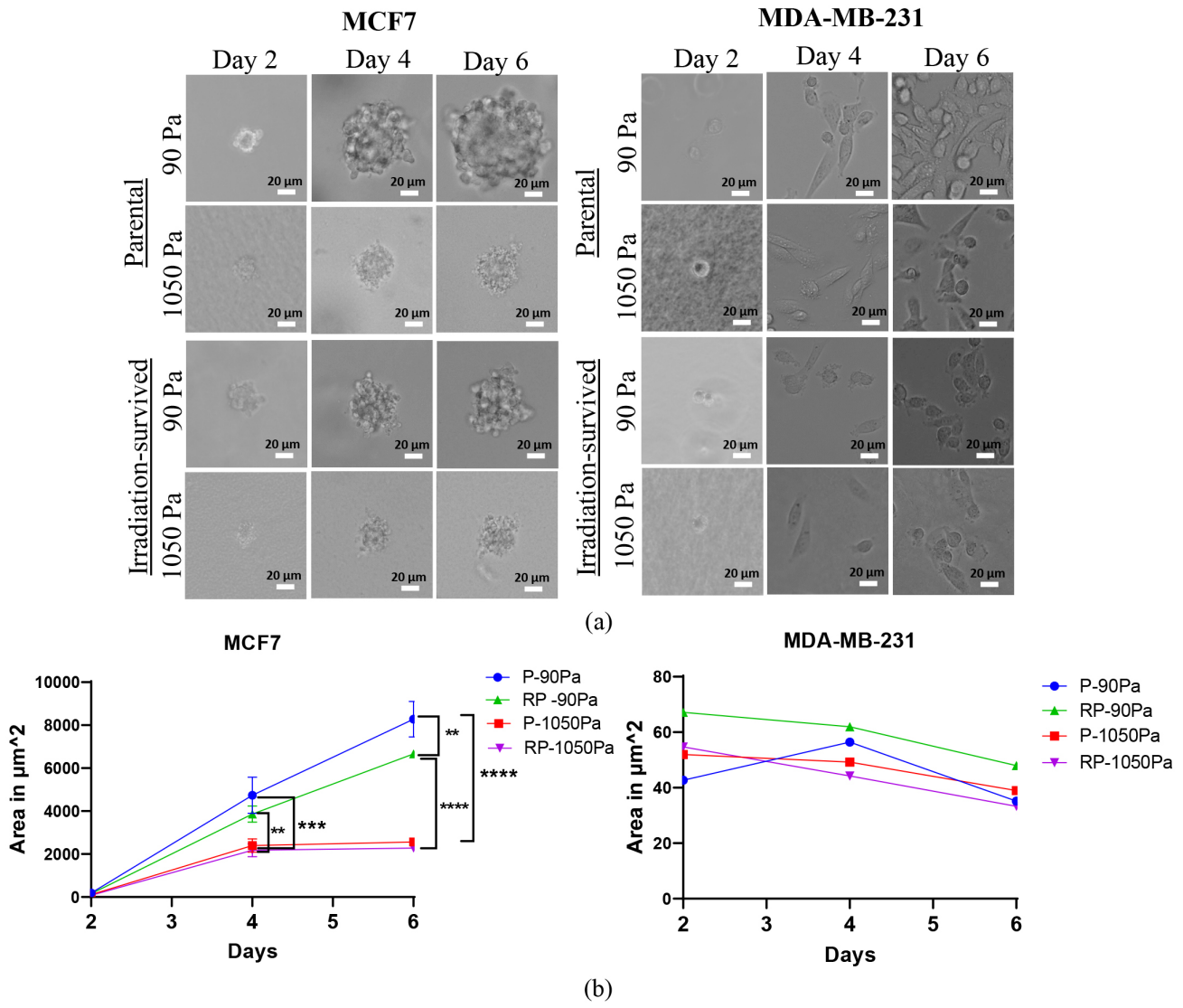

Fig. 6. Analysis of tumor spheroid growth in a 3D fibrin matrix. Images (a) and quantification of the area (b) of multicellular tumor spheroids grown within 90 and 1050 Pa 3D fibrin gels during the culture course of parental (P) and proton irradiation-survived (RP) MCF7 and MDA-MB-231 cells on days 2, 4, and 6. Statistical significance calculated by two-way ANOVA with Tukey correction for multiple comparisons. ** $p \leq 0.01$, *** $p \leq 0.001$, **** $p \leq 0.0001$. Data are means ± SD from three independent experiments. Scale bar 20 µm.

tive (SA-β-gal+) cells on the first day of analysis was 10% and 30% in MCF7 and MDA-MB-231 (Fig. 3a) cells, respectively, while not exceeding 2% during the subsequent 7 days of incubation.

PBI caused a significant increase in the proportion of SA-β-gal+ cells by ~55% and 50% in MCF7 and MDA-MB-231 cells, respectively (Fig. 3a). On day 3 after irradiation, the proportion of the SA-β-gal+ MCF7 cells was 27%, which further increased to 55% on day 7 (Fig. 3a). In contrary, only 5% of MDA-MB-231 cells were SA-β-gal+ on day 3, increasing to 20% (Fig. 3a) on day 7 after irradiation.

Entosis has recently been proposed as another potential survival mechanism in cancer cells exposed to radiation-induced stress [46]. BC has been found to have a high level of entosis competence, with entotic figures being observed in both primary tumors and metastatic lesions [47–49]. Despite this, little is currently known about the extent and effectiveness of the entosis process in human BC cell lines following proton irradiation.

Non-irradiated MCF7 cells exhibited a very low fraction ($\leq$0.5%) of entotic cells when cultured under adherent and serum-rich conditions. As expected, entosis was exclusively observed in proton-irradiated MCF7 cells (Fig. 3b), but was absent in MDA-MB-231 cells under the same conditions. Interestingly, the majority of entotic MCF7 cells were positive for β-galactosidase, indicating an association with the SIPS phenotype (Fig. 3b, indicated by arrows). Al-

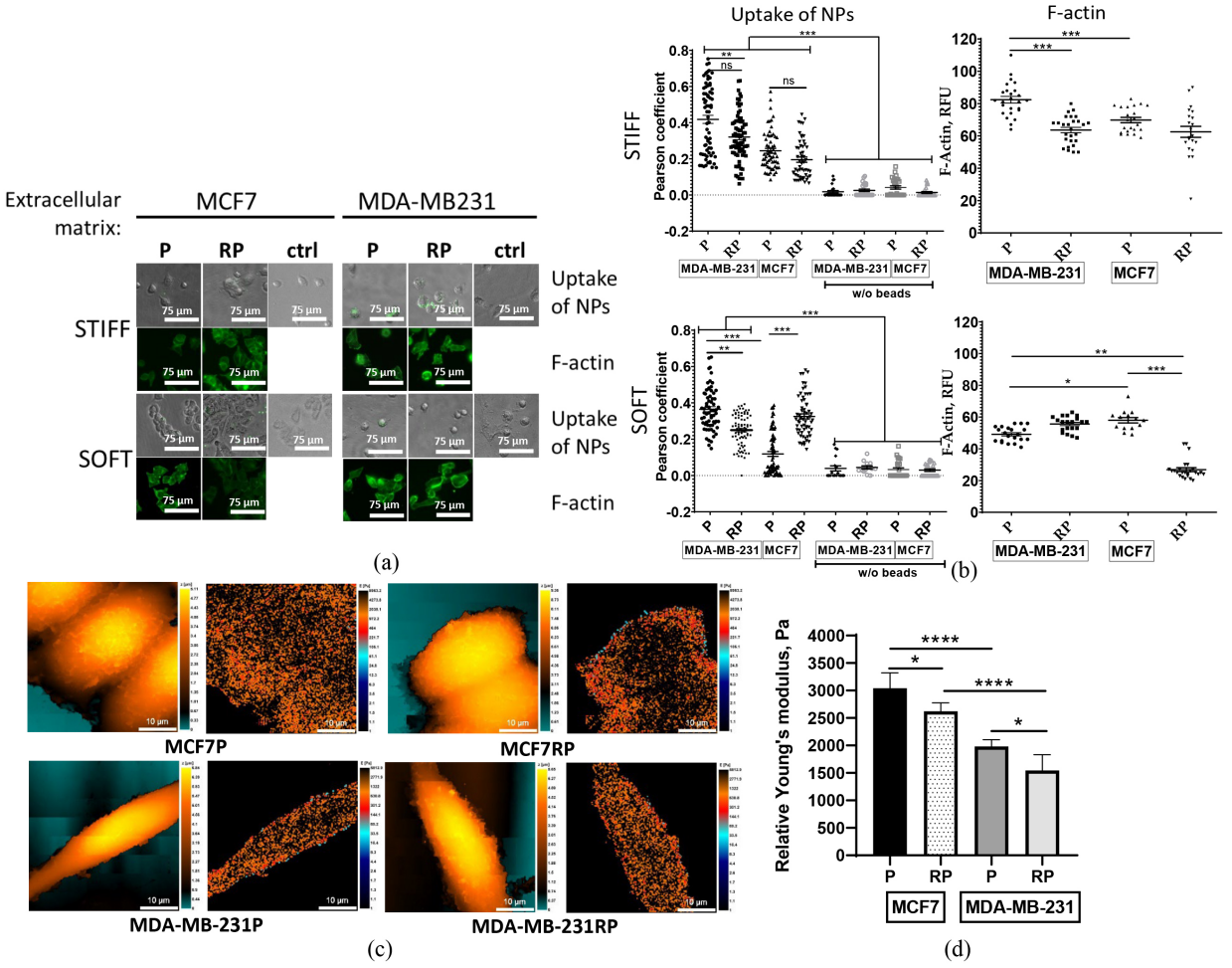

Fig. 7. Analysis of nanoparticles association and F-actin expression by parental (P) and proton irradiation-survived (RP) MCF7, and MDA-MB-231 cells seeded on 2D stiff plastic or a soft fibrin (90 Pa) layer following their pre-cultivation on either 2D stiff (plastic) or 3D soft fibrin gel, respectively. Representative pictures of cellular nanoparticles (NP) association test and F-actin phalloidin staining (a). The quantitative comparison of cellular NP uptake efficiency was calculated based on quantitative co-localization (Pearson's and overlap coefficients, scatter slope) of fluorescent nanoparticles, and integrated fluorescence intensities (RFUs) of F-actin filaments (b). Scale bar 75 µm. Topography (left) and stiffness (right) mapping images obtained using scanning ion-conductance microscopy (SICM) on breast cancer cell lines (c). Scale bar 10 µm. Average relative Young's modulus calculated as a weighted mean for each cell and then averaged across all measured cells (d). Statistical significance calculated by Student's *t*-test. * $p < 0.05$, ** $p \leq 0.01$, *** $p \leq 0.001$, **** $p \leq 0.0001$, ns, not significant. Data are means of three independent experiments ± SD. F-actin, filamentous actin.

though the proportion of entotic cells remained low under adherent and serum-enriched conditions, it significantly increased over time following proton irradiation (Fig. 3c).

Thus, the lower levels of the SA-β-gal senescence marker (Fig. 3a), the absence of entosis, and the less efficient DNA DSB repair mechanisms likely contribute to the heightened sensitivity of MDA-MB-231 cells to high-LET irradiation compared to MCF7 cells.

3.4 Influence of High-Let Irradiation on 2D Cell Migration Inside a Monolayer and Confined Migration of Cancer Cells

The remarkable biophysical properties of metastatic migrating cells, such as their exceptional motility and deformability, enable them to navigate through physical confinements created by neighboring cells or extracellular matrix (ECM) [29,50]. The "scratch" test, also known as the wound healing assay, is a widely employed *in vitro* technique serving as a valuable tool allowing for the real-time visualization and quantification of 2D cell migration inside a monolayer cultured in serum-depleted medium (1% FBS) for 24 hours post-wound formation.

Non-irradiated parental MDA-MB-231 cells exhibited nearly double the migration within a monolayer as compared to non-irradiated MCF7 cells (Fig. 4a,b). Both MDA-MB-231RP and MCF7RP cell sublines demonstrated enhanced wound healing abilities compared to their non-irradiated parental cell lines (Fig. 4b).

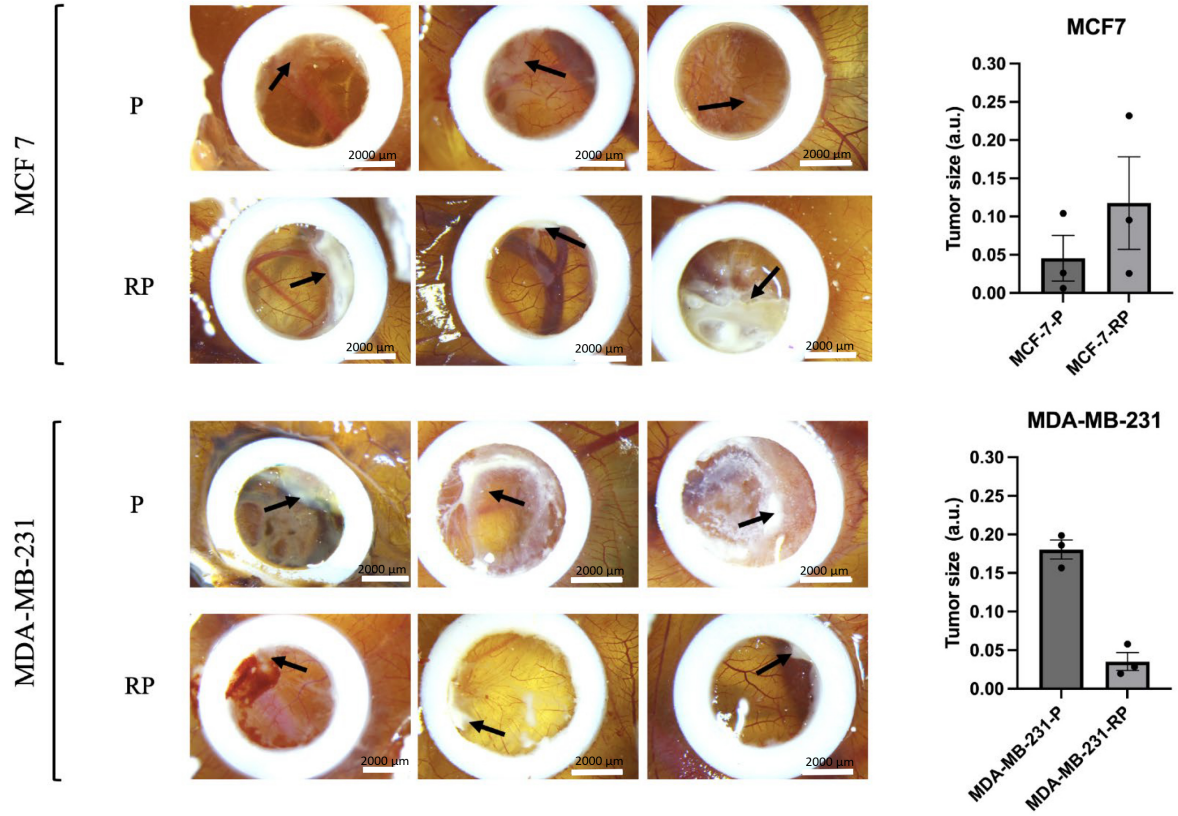

Fig. 8. The chick embryo chorioallantoic membrane (CAM) model was employed to assess the tumorigenic potential of BC cells. Representative images depict tumors that developed by embryonic day 16 in an *in vivo* CAM tumorigenicity assay, comparing parental (P) MDA-MB-231 and MCF7 cells with their proton irradiation-survived counterparts (RPs). Black arrows indicate tumor formation sites. Scale bar 2000 µm. The right panel illustrates the comparative tumor sizes between the P and RP groups. Statistical significance calculated by the Mann–Witney U-test. Values represent data from individual tumors with the mean ± SEM (n = 3 per sample).

Using the classical transwell or Boyden Chamber assay, we evaluated a fraction of cancer cells that were confined in a physically restricted microenvironment. These cells were allowed to migrate through a membrane with 8 µm pores, which are significantly smaller than their size (19–21 µm), while following a gradient of serum concentration formed between the upper and lower chambers (Fig. 4c). In concordance with the 2D monolayer motility data, the non-irradiated MCF7 cells possess a significantly lower fraction of confined-migrating cells compared to MDA-MB-231 cells (Fig. 4d). In contrast to the 2D monolayer motility data, the MDA-MB-231RP subline, which survived high-LET exposure, exhibited a most prominent (14-fold) decrease in the number of confined-migrating cells compared to the MCF7RP (10-fold) subline (Fig. 4d).

3.5 Acquisition of EMT Traits by High-LET Irradiation-Survived Cell Sublines

EMT is a crucial biological process involved in various physiological and pathological conditions including cancer metastasis and invasion. EMT is characterized by the transition of epithelial cells into a mesenchymal phenotype, leading to changes in cellular morphology, gene expression, and functional properties. During classical EMT, epithelial markers such as E-cadherin are downregulated, while mesenchymal markers, including N-cadherin, Vimentin, and SNAIL are upregulated [51].

Unexpectedly, high-LET exposure led to an increase in E-cadherin expression in MCF7RP cells, while no significant effect was observed in MDA-MB-231RP cells compared to their respective non-irradiated parental controls (Fig. 5a, **Supplementary Fig. 1a**). Additionally, we observed a significant decrease in N-cadherin expression in MCF7RP cells ($p < 0.05$), whereas its expression was significantly increased in MDA-MB-231RP cells compared to parental cells (Fig. 5b, **Supplementary Fig. 1b**). Vimentin expression was undetectable in both parental and MCF7RP cells, while its high expression remained unchanged between parental and MDA-MB-231RP cells (Fig. 5c, **Supplementary Fig. 1c**). SNAIL, a key transcriptional repressor of E-cadherin expression [52], showed an unexpected increase in expression in both MCF7RP and MDA-MB-231RP cells, although the change did not reach statistical significance (Fig. 5d, **Supplementary Fig. 1d**).

3.6 Fibrin Gel Stiffness Reveals Mechanobiological Difference Between Proton Irradiation-Survived Cancer Cells

Soft 3D fibrin gels can select highly tumorigenic cells and support their growth without differentiation. Only soft tumor cells, not stiff ones, can form spheroid colonies [53]. In this study, untreated parental MCF7 and MDA-MB-231 cells, along with their isogenic proton irradiation-survived descendants were seeded in 3D fibrin gels with stiffness levels of 90 Pa and 1050 Pa. Previous research has demonstrated that stiffness of 90 Pa promotes cancer stemness [54], whereas 1050 Pa approximates the stiffness of healthy breast tissue [55]. Bright-field digital images of growing spheroids were captured under a microscope on days 2, 4, and 6 post-seeding (Fig. 6a). The area of each spheroid colony was subsequently measured using ImageJ software.

The mean area of compact MCF7 spheroids (of both irradiation-survived and parental cells) increased with time becoming significantly ($p < 0.0001$) higher in low (90 Pa) compared to higher (1050 Pa) stiffness gel by day 6 after seeding (Fig. 6b). When cultured on a fibrin gel with a stiffness of 90 Pa, MCF7RP cells exhibited a remarkable ($p < 0.01$) reduction in spheroid size when compared to non-irradiated parental cells. This observation suggests a reduced soft cell population that survives after proton exposure. In contrast, it was not evident in the gel with a stiffness of 1050 Pa, where no difference in colony area was observed at any time after seeding (Fig. 6b).

Meanwhile, MDA-MB-231 cells, both non-irradiated parental and irradiation-survived, formed only small diffuse spheroid colonies that remained almost unchanged in size over time, regardless of fibrin gel stiffness (Fig. 6b). By day 4 post-seeding, these cells had even degraded the fibrin gel and were predominantly found adherent to the bottom of the 6-well plate. Since cancer cells are known to secrete matrix metalloproteinases (MMPs) to degrade the basement membrane and facilitate invasion into the stromal matrix, we hypothesized that MDA-MB-231 cells mediate protease-driven degradation of the fibrin gel. However, the addition of the MMP inhibitor Marimastat on the first day of culturing had little to no effect on fibrin gel degradation in both parental and irradiation-survived MDA-MB-231 cells (data not shown).

3.7 High-LET Irradiation Affects Nanoparticle Uptake and Extracellular Mechanosensation by Breast Cancer Cells

After observing the differing abilities of proton irradiation-survived MCF7RP and MDA-MB-231RP cells in 2D migration in a monolayer and confined migration (Fig. 4), we aimed to further evaluate their metastatic potential in comparison to their parental counterparts. One emerging method for assessing metastatic potential is the NP test, which examines cellular nanoparticles (NP) uptake. This approach explores the relationship between cell migration and cancer cell endocytosis, emphasizing the role of the actin cytoskeleton [37].

To investigate the well-documented influence of ECM on cytoskeletal changes, cells were either pre-cultivated on rigid plastic surfaces ($>10^7$ kPa) or allowed to grow in a pliable 3D fibrin gel (90 Pa). Following this, the amount of cell-associated NPs was evaluated in two-dimensional (2D) settings, where cells pre-cultivated on plastic surfaces were adhered to a rigid plastic surface and cells from 3D fibrin gel were seeded onto a soft fibrin gel layer (90 Pa). The amount of single cell-associated NPs was quantified subsequently using high-content imaging and analysis techniques, as outlined in our prior research [56]. The cells without NPs were used as the negative controls (see Fig. 7a).

Regardless of microenvironment stiffness during pre-cultivation and NP association, the highly metastatic parental MDA-MB-231 cells exhibited significantly higher NP association efficiency compared to non-metastatic parental MCF7 cells (Fig. 7b). In contrast, the efficiency of NP association in PBI-survived MCF7RP and MDA-MB-231RP cells displayed a clear dependence on microenvironment stiffness. MDA-MB-231RP cells exhibited a marked reduction in NPs association compared to their parental counterparts ($p < 0.01$) when both exposure and NP-cell interactions occurred in a soft microenvironment (Fig. 7b, lower panel). However, in stiff conditions, no significant changes in NP association were observed (Fig. 7b, upper panel). Conversely, MCF7RP cells demonstrated a striking increase in NP uptake compared to their parental cells ($p < 0.001$) under soft microenvironment conditions (Fig. 7b, lower panel), whereas NP association remained unchanged in stiff environments (Fig. 7b, upper panel). These findings indicate that high-LET irradiation alters the mechanosensation of PBI-survived MCF7RP and MDA-MB-231RP cells, modifying their ability to perceive the microenvironment stiffness. This, in turn, results in substantial changes to their mechano-biological properties, ultimately influencing their metastatic potential.

Next, we investigated the hypothesis that the microenvironment stiffness experienced by BC cell lines during culture influences their own cytoskeletal changes. Given that filamentous actin (F-actin) plays a crucial role in determining cell stiffness, one of the important biophysical features of malignant cells [56], we undertook a comprehensive analysis utilizing phalloidin staining of F-actin.

Both parental (P) MDA-MB-231 and proton irradiation-survived (RP) MCF7 cells cultured on a stiff plastic (Fig. 7a,b upper panels) exhibited significantly greater levels of cellular F-actin expression than those grown on a soft fibrin layer (Fig. 7a,b lower panels). High-LET irradiation-survived MCF7RP cells demonstrated a notable increase in softness compared to their parental cells, as evidenced by a significant reduction in F-actin expression, but only within a softer microenvironment (Fig. 7b). Conversely, MDA-MB-231RP cells

exhibited greater stiffness in comparison to their parental counterparts, although the difference was not statistically significant when maintained in the same microenvironment (Fig. 7b, lower panels).

SICM was used to confirm the mechanical properties of the cell membrane by obtaining both topographical and stiffness mapping images of parental and PBI-survived cell sublines (Fig. 7c). We did not observe significant morphological changes following PBI exposure. The characteristic Young's modulus revealed that parental MCF7 is significantly stiffer than MDA-MB-231 cells, which corroborates previous studies [57,58]. Furthermore, both the PBI-survived cell sublines MCF7RP and MDA-MB-231RP exhibited a statistically significant decrease in stiffness following irradiation (Fig. 7d). This finding aligns with our data on NP uptake and F-actin expression in cells cultured within a stiff microenvironment (Fig. 7b, upper panel), suggesting a correlation between reduced stiffness, F-actin expression and increased 2D collective migration of PBI-survived cells (Fig. 4b).

3.8 High-LET Effects on In Vivo Breast Cancer Tumorigenesis

The chick embryo CAM model presents a compelling *in vivo* alternative for tumor engraftment. Its vascularized membrane fosters robust tumor growth while the chick embryo's immune system remains underdeveloped until embryonic day 16 (E16), making it an ideal environment for such research [59–61]. In this *in vivo* model, we sought to investigate the comparative tumorigenic potential of parental (P) MDA-MB-231 and MCF7 cells alongside their proton irradiation-survived counterparts (RPs).

By E16, the parental (P) MDA-MB-231 cells formed a substantially larger tumor mass organization characterized by a well-organized tumor–stroma that exhibited a white-opaque appearance and marked revascularization through CAM vessels (see Fig. 8, lower panel, marked by the black arrow). The implanted parental MCF7 cells exhibited a well-organized structure within small clusters, particularly near the CAM vessels. There was little indication of tumor mass organization, accompanied by surrounding mesenchymal and inflammatory reactions (refer to Fig. 8, upper panel).

Fig. 8 clearly illustrates that the proton irradiation-survived (RP) variant of MDA-MB-231RP cells displayed only minimal tumor growth (indicated by black arrow), highlighting a ~6-fold decrease in their tumorigenic potential *in vivo* compared to parental MDA-MB-231 cells. On the other hand, MCF7RP cells exhibited a more pronounced (~3-fold higher size) organization of tumor mass compared to their parental cell line. These data suggest that high-LET proton irradiation substantially impacts the tumorigenic ability of these cells when compared to their syngeneic parental counterparts.

4. Discussion

BC is the most common cancer type among women globally and the second most common overall, making it a major contributor to cancer-related mortality among women worldwide [62]. While PT shows a promising approach for the treatment of BC, there is still a substantial knowledge gap regarding the cellular and molecular responses of BC cells to proton irradiation. In this study, we investigated the RBE of PBI for two BC cell lines, MCF7 and MDA-MB-231 (Fig. 1a), using a clonogenic assay. The RBE of PBI in MCF7 and MDA-MB-231 (Fig. 1b) cell lines for the 10% cell survival fraction (i.e., SF = 0.1) was found to be 1.7 and 1.75, correspondently, demonstrating the superior efficacy of PBI in eliminating cancer cells compared to conventional photon irradiation. Notably, the MDA-MB-231 cells demonstrated the lowest clonogenic survival rates after high LET irradiation when compared to the MCF7 cell line. This finding is consistent with previous observations [34]. The large differences in the slopes of D10% for proton and D10% for X-ray curves in both BC cell lines show that both physical and biological factors are important in determining the sensitivity of BC cells to radiation based on LET.

High-LET radiation, such as PT, induces complex clustered DNA lesions including non-DSB damage surrounding DSB. These lesions are often inefficiently repaired or remain unrepaired, contributing to the greater mutagenic and cytotoxic effects observed in irradiated cells [63,64]. Our observed differences in the sensitivity of TNBC (MDA-MB-231) and ER-positive (MCF7) cell lines to PT raise questions regarding the DDR protein signatures associated with cellular sensitivity to high- versus low-LET radiation. The expression changes of these DDR proteins following ionizing radiation exposure have been extensively studied by us and other researchers [65–69]. Earlier transcriptomic studies identified several key genes involved in BC cell radiosensitivity to high-LET radiation including Rad51 [70], along with four additional effectors, recently confirmed [71].

The present study demonstrates that PBI induces significantly different effects on DNA DSBs in two BC cell lines, as evidenced by the immunofluorescent analysis of γH2AX protein. Notably, after 1 hour of 2 Gy irradiation, the number of γH2AX foci was higher in MDA-MB-231 cells compared to MCF7 cells (Fig. 2a,b). These differing responses likely stem from the fundamental genetic and molecular differences between the two cell lines. MDA-MB-231, a more aggressive TNBC subtype, is known for its increased genomic instability and a greater propensity for accumulating DNA damage. Similar findings were reported by Alkhansa Mahmoud *et al.* [34], who demonstrated that MDA-MB-231 cells exhibit greater radiosensitivity than MCF7 cells, showing significantly higher γH2AX expression via Western blot analysis. In our study, MDA-MB-231 cells also exhibited increased levels of all

three key DDR proteins 48 hours post-irradiation with PBI (Fig. 2). This suggests the presence of residual RIF that remains unresolved has the potential to cause significant cellular damage. Consequently, the decreased clonogenic survival of MDA-MB-231 cells following PBI (Fig. 1b) can be attributed to their inefficient DNA damage repair mechanisms. This is further supported by the persistent accumulation of unresolved RIF of three critical DDR proteins after irradiation.

Tumor repopulation and metastasis following IR remain major challenges in the successful effective elimination of cancer. To address this, we aimed to investigate the characteristics of BC cells that survive PBI, focusing on their ability to grow and spread. MCF7 and MDA-MB-231 cell lines were exposed to a single lethal dose (6 Gy) of PBI and allowed to recover for 3–4 weeks. All subsequent experiments (refer to Sections 2.6–2.12) were conducted to assess the survival characteristics of their progeny, now designated as the MDA-MB-231RP and MCF7RP sublines, in comparison to their parental isogenic counterparts.

Even when DNA damage remains unaddressed, tumor cells can evade programmed cell death and survive proton-based treatment by entering various forms of dormancy including senescence. Despite being permanently arrested in proliferation and lacking the ability to divide, senescent cells exhibit resistance to apoptosis, sustained metabolic activity, an SIPS phenotype, and the ability to alter their surrounding microenvironment [72]. Studies, including our own, have demonstrated that the IR dose plays a crucial role in determining whether irradiated cancer cells undergo senescence or apoptosis [67,73–76]. This phenomenon is closely associated with the extent of DNA damage and the functionality of the DDR network. Entosis has recently been proposed as another potential survival mechanism in cancer cells exposed to radiation-induced stress [46]. Through this process, tumor cells compete with the winning cells engulfing and eliminating weaker neighboring cells. Additionally, there is evidence suggesting that stress conditions can trigger a fatal form of entosis, where internalized cell undergoes lysosomal digestion. This has been observed in approximately 30% of MCF7 cells grown in suspension, while under the same conditions, no entotic events were detected in MDA-MB-231 cells [77]. However, under fully adherent conditions, certain cancer cells may undergo a vital form of entosis instead [46]. BC is known to exhibit a high level of entosis competence, with entotic figures observed in both primary tumors and metastatic lesions [47–49]. Here, for the first time, we report that the entotic program is exclusively activated in proton irradiation-survived MCF7 cells (Fig. 3c) under fully adherent conditions. In contrast, this phenomenon remains absent in MDA-MB-231 cells grown under identical conditions. Remarkably, a majority of entotic MCF7 cells were positive for SA-β-gal, a well-established marker of SIPS (Fig. 3b, indicated by arrows). Although the proportion of entotic cells was low under adherent, serum-enriched conditions, it dramatically increased over time following proton irradiation (Fig. 3c). Collectively, the increased presence of SA-β-gal+ cells and the occurrence of entosis in TP53-competent MCF7 cells likely mirror a more precise and efficient DNA repair response following high-LET irradiation. This contrasts with TP53-deficient MDA-MB-231 cells, which lack efficient DNA repair responses to support these compensatory survival mechanisms. These findings suggest that entosis may play a crucial role in BC progression, with potential implications for therapeutic targeting. Entosis is often associated with more aggressive cancer phenotypes, which correlate with poor prognosis and lower survival rates [78–80]. Previously, we observed a similar increase in entosis linked to TP53 phenotype in adherently propagated NSCLC cell lines following low-LET irradiation [81].

Our observed significant differences in clonogenic survival, DDR, motility, and invasiveness in response to PBI raise the question of whether the key molecular effectors driving these processes are also differentially engaged in MCF7RP and MDA-MB-231RP sublines. Recent transcriptomic studies have indicated that following PBI, the TP53 signaling pathway was identified as the most statistically significant pathway activated in MCF7 cells [71,81]. This activation emphasizes its crucial role in balancing cell survival and death after irradiation. In contrast, the EMT pathway was among the top five activated pathways in MDA-MB-231 cells following PBI [12,71]. Our findings collectively indicate that high-LET radiation induces a divergent, either non-classical (hybrid) EMT or mesenchymal-to-epithelial transition (MET) phenotypes in irradiation-survived sublines. Based on classical marker expressions, MCF7RP (TP53-competent) cells exhibited more likely a MET phenotype, characterized by lowering N-cadherin and Vimentin levels and a significant increase in E-cadherin expression. Conversely, MDA-MB-231RP (TP53-deficient) cells intensified their mesenchymal phenotype, showing significant upregulation of N-cadherin and a marginal increase in SNAIL, despite unchanged levels of Vimentin and E-cadherin expressions. This hybrid EMT phenotype induced by high-LET irradiation in MDA-MB-231RP sublines significantly enhanced 2D collective migration in monolayer (Fig. 4b), but not the 3D confined migration (Fig. 4d) compared to their parental counterparts. This raises the question of whether there is a direct correlation between the EMT-MET phenotype, migration, and invasion of cancer cells. For instance, previous study have demonstrated that EGFR inhibition in prostate cancer epithelial cells reduced their migration but not invasion [82]. Additionally, defining EMT solely based on a limited set of classical markers, as was carried out in the current study, may not provide a comprehensive characterization of the process. Initially studied in the context of embryonic development, EMT research has since evolved into a major focus

in cancer biology. However, the variability and adaptability of EMT programs have not been adequately addressed [39]. Our study highlights that during the EMT–MET process, cancer cells often co-express epithelial and mesenchymal markers, frequently failing to undergo complete EMT transition. This suggests that partial (or hybrid) EMT states are more common than previously thought, reinforcing the idea that traditional EMT markers, such as E-cadherin, N-cadherin, and Vimentin, may not fully capture the complexity of EMT in cancer cells [39].

The unique biophysical properties of metastatic migrating cells, including their exceptional motility and deformation capabilities, enable them to navigate through the physical constraints imposed by adjacent cells and the ECM [29,50]. Solid tumors are influenced by mechanical forces from the surrounding tissue, which induce tumor cells' deformation, significantly impacting their migration, division, and survival [83]. A strong correlation exists between cancer cell deformability and malignancy, with a reduction in cancer cell stiffness, as measured by the Young's modulus [84]. Stiffness defined as the ratio of stress to deformation describes a cell's ability to resist shape changes. In various cancer types, undifferentiated tumorigenic cells are generally softer than their differentiated counterparts [85]. Notably, metastatic cancer cells isolated from the pleural fluids of BC patients exhibited over 70% lower stiffness compared to benign reactive mesothelial cells [86]. During entosis, highly deformable soft cells are more efficient in engulfing and outcompeting stiffer neighboring cells, a process driven by RhoA and actomyosin activity [87]. Our current findings indicate that high-LET radiation induces entosis in MCF7 cells (Fig. 3c), while it does not affect MDA-MB-231 cells. The difference suggests inherent variations in cellular stiffness, which was confirmed by our SICM measurements of the two cell lines. Interestingly, the tendency for entosis did not show any correlation with cell stiffness as assessed by SICM (Fig. 7c,d). Of note, the descendants of PBI-survived both MCF7 and MDA-MB-231 cells further decreased their cellular stiffness.

ECM stiffness plays a crucial role in various cellular processes, including growth, proliferation, migration, immunity, malignant transformation, metabolic reprogramming, and apoptosis [88]. In the present study, we investigated the effects of ECM stiffness on MCF7 and MDA-MB-231 cells. Our findings reveal a compelling inverse relationship between the volume of parental MCF7 spheroids and the stiffness of the fibrin gel used for encapsulation (Fig. 7a,b). This observation aligns with a recent study that reported similar results using MCF7 cells cultured on a linear stiffness gradient of GelAGE [89]. For the first time, we demonstrate that proton irradiation affects the spheroid-forming (tumorigenic) abilities of MCF7 cells, as revealed by spheroid culturing within a 3D soft (90 Pa) fibrin gel microenvironment (Fig. 6). Liu *et al.* [53] previously showed that softer fibrin gels (90 Pa) promote tumorigenicity and stemness features in melanoma cells, leading to primary and secondary tumor formation in animal models. In contrast, a microenvironment that mimics the mechanical properties of healthy breast tissue (1050 Pa) [90] likely plays a protective role in maintaining cell properties, making it difficult to distinguish MCF7RP from parental cells based on spheroid area. Our data also highlight the limitations of using soft fibrin gels to differentiate highly deformable and potentially more metastatic cancer cells, particularly when these cells (e.g., both parental and proton irradiation-survived MDA-MB-231 cells) secrete gel-degrading factors that compromise ECM stiffness (Fig. 6). In our current study, we did not aim to investigate the nature of fibrin gel-degrading activity. The role of matrix metalloproteases (MMPs) was not supported, as using Marimastat, a broad-spectrum inhibitor of MMPs, did not affect our study results. Indeed, plasmin, a serine protease, can break down cross-linked fibrin multimers within a clot in the peripheral circulation. Aprotinin, a proteolytic enzyme inhibitor, has been previously demonstrated to slow fibrinolysis [91]. Aprotinin is a natural serine protease inhibitor that blocks various proteases, such as plasmin, urokinase, protein C, elastase, cathepsin, and kallikrein. Aminocaproic acid, another plasmin-specific inhibitor, could be further utilized in experiments involving MDA-MB-231 cells grown in fibrin. Consequently, the influence of these plasmin inhibitors warrants further investigation. Together, these findings prompted us to explore alternative methods for comparing the mechano-biological characteristics that underlie differences between high-LET radiation-survived BC cell lines.

F-actin is a critical component of the cytoskeleton playing a key role in determining cell the mechanical properties of cells, particularly stiffness [56]. Disrupting actin stress fibers eliminates variations in cell stiffness, chromatin stretching, and gene upregulation in response to mechanical forces [92]. Previous studies have shown that beads coated with a synthetic peptide containing the Arg-Gly-Asp (RGD) sequence bind to cells via integrin–actin linkages. When tethered by tense F-actin bundles (stress fibers), these bundles primarily resist bead rotation or movement under stress, serving as an index of cell stiffness. Disrupting of F-actin bundles reduces tethering, leading to decreased resistance to bead rotation and significantly lower cell stiffness [93,94]. To examine how ECM stiffness affects cytoskeletal (F-actin) changes and their link to metastatic potential, we conducted a nano-bead association assay to assess the ability of MCF7RP, MDA-MB-231RP, and their parental cell lines to encapsulate carboxylate-modified fluorescent NPs (see Fig. 7a,b). This encapsulation was used as an indicator of their pro-metastatic phenotype [37]. Regardless of the microenvironment stiffness, the highly metastatic parental MDA-MB-231 cells exhibited significantly higher association efficiency than non-metastatic parental MCF7 cells (Fig. 7b), consistent with previous findings [37]. Next, we found that both parental

cell lines demonstrated mechanosensation—the ability to perceive ECM stiffness and translate that information into F-actin expression (Fig. 7b, right upper vs. lower panels). Our results show that high-LET irradiation alters the mechanosensation of proton-irradiated MCF7RP and MDA-MB-231RP cells, affecting their perception of microenvironment stiffness. This, in turn, leads to substantial modifications in their mechano-biological characteristics, ultimately impacting their metastatic potential. This finding aligns with recent observations in non-metastatic MCF7 cells and confirms earlier predictions [95]. The F-actin cytoskeleton is a highly organized composite structure composed of cortical actin and F-actin stress fibers, both of which play a crucial role in cell mechanics, including division and migration [96]. We present novel evidence that MCF7RP and MDA-MB-231RP cells that survived high-LET proton irradiation exhibit an inverse correlation between F-actin expression—an indicator of cell stiffness—and NP uptake, a marker of metastatic potential. Our findings underscore the significant impact of relationships. In soft microenvironments, high-LET irradiation survivors from the highly aggressive and metastatic MDA-MB-231 cell line exhibit a significant reduction in metastatic potential, as manifested by lowering NP uptake *in vitro*. Conversely, high-LET irradiation survivors from the non-metastatic MCF7 cell line appear to enhance this trait under the same microenvironment. These unexpected *in vitro* results prevented us from drawing definitive conclusions regarding the tumorigenic and metastatic potential of the proton irradiation-survived sublines.

This prompted us to directly compare the tumorigenicity of MDA-MB-231RP and MCF7RP cell sublines using an *in vivo* model. The chick embryo CAM, *in ovo* model, is a promising alternative *in vivo* system, well-suited for tumor engraftment due to its extensive vascularization, which supports tumor growth, and the lack of a fully developed immune system in the chick embryo until E16 [59–61]. This model has been widely used to study cancer biology in various contexts, including tumorigenicity, angiogenesis, metastasis, and anticancer drug testing, and serves as a robust alternative to simple organoids and costly patient-derived xenograft (PDX) mouse models [97]. *In ovo* experiments offer a low-cost, time-efficient approach, allowing tumor growth assessment within a relatively short 16-day period, with being for further analysis [59].

In this model, the parental highly aggressive and metastatic MDA-MB-231 cells formed substantial cell clusters characterized by a well-organized tumor–stroma that exhibited a white-opaque appearance and marked revascularization through CAM vessels (see Fig. 8, the black arrow in the upper P panel). In stark contrast, when we grafted parental MCF7, we observed minimal evidence of organized tumor mass formation, alongside notable angiogenic and vasculogenic effects in the surrounding tissue (refer to Fig. 8, the black arrow in the upper panel). The data show strong consistency with previously published findings from other research groups [98,99]. Consistent with our *in vitro* NP uptake findings under soft microenvironments, MDA-MB-231RP cells displayed only minimal tumor growth (Fig. 8, the black arrow in the lower RP panel), indicating a substantial decrease in their tumorigenic potential *in vivo*. In contrast, MCF7RP cells generated larger tumors compared to their parental cell line (Fig. 8, the black arrow in the upper RP panel), a result that also aligns well with our *in vitro* findings regarding nanoparticle uptake in softer microenvironments. It is important to consider that the effects observed in MCF7 cells may be specific to either cell type or the species, as parental MCF7 cells exhibited significant alterations in their molecular profile after grafting onto the CAM, leading to the acquisition of a more aggressive phenotype. Notably, they transitioned to a triple-negative status and initiated EMT, as indicated by the expression of vimentin and the concurrent loss of β-catenin and CK18 [100,101]. One limitation of this study is that we did not initially anticipate investigating molecular phenotype changes in MCF7RP cells post-engraftment onto the CAM. A more comprehensive analysis is needed to fully understand EMT and metastatic alterations induced by both PBI and CAM engraftment, which may provide insights into their role in cancer progression and therapy resistance. Our current findings strongly support the idea that ECM stiffness significantly influences EMT and tumorigenesis in BC cells following proton irradiation. Our upcoming comparative study, incorporating both *in ovo* and *in vivo* methodologies, aims to further explore molecular mechanisms underlying this potential phenotypic switch. Additionally, our SICM findings suggest that MDA-MB-231RP and MCF7RP cells exhibit reduced stiffness compared to their isogenic parental lines.

The effects of ionizing radiation on the cytoskeleton-mediated mechanobiological properties of tumor cells are well-established and thoroughly researched [102]. The investigation into how PBI affects these properties has just started, leading to new insights and discoveries. While mechanosensation of the tumor microenvironment (TME) is usually performed through the activation of surface mechanosensors such as integrins [103], transient receptor potential (TRP) ion channels [104], and the yes-associated protein (YAP) and the transcriptional coactivator with PDZ-binding motif (TAZ) molecular complex [105], actin cytoskeleton plays an essential role as a mechanotransducer. In this role, it converts physical stress into biochemical signals, which affect cell actions like division, adhesion, and migration. X-ray irradiation induced a depolymerization of the actin filaments and, consequently, a decrease in their elastic modulus that ultimately led to the augmentation in the migratory and invasive abilities of tongue squamous cell carcinoma (TSCC) cells [106]. Alterations in the cytoskeletal network were observed, indicated by a reduced signal intensity of actin fibers. These data correlate well with our

results. Furthermore, our study clearly indicates that PBI also affects mechanosensation, so that highly metastatic tumor cells surviving proton irradiation (MDA-MB-231RP) are more likely to metastasize (indicated by NP uptake) in a rigid TME compared to when they are in a softer TME. While this study did not focus on the direct impact of PBI on mechanosensor functions, it clearly requires further investigation.

PT for BC is characterized by higher costs and limited accessibility compared to traditional photon therapy. Clinical trials have not consistently shown that PT is better than photon therapy, so radiation oncologists must evaluate patients carefully. This evaluation is crucial to ensure that the dosimetric advantages of proton therapy translate into meaningful clinical benefits.

There are no systematic reviews or clinical trials comparing proton therapy's effects on different molecular subtypes of BC. Studies have explored how breast cancer cell lines react to proton irradiation, particularly regarding DNA repair [107] and molecular pathways [108]. These studies examine how various cell lines respond to PT, but they do not address clinical outcomes for different breast cancer subtypes.

Our research indicates that PT may effectively treat TNBC by studying cancer recurrence in live models. In particular, our results indicate that highly metastatic tumor cells surviving proton irradiation (MDA-MB-231RP) are more likely to metastasize (indicated by NP uptake) in a rigid microenvironment compared to when they are in a softer environment. From a clinical standpoint, combining treatments that soften tumor tissue with proton therapy may reduce the risk of metastases in TNBC patients following radiation therapy. However, this requires further confirmation *in vivo* models. There is still a strong need for thorough reviews and clinical trials to compare the outcomes of PT in various BC subtypes. Such studies would help determine whether PT provides unique benefits for specific subtypes and inform personalized treatment strategies.

5. Conclusions

PBI appears to be a key factor in modulating the mechanosensation of two distinct BC cell lines. In softer ECM environments, survivors of non-metastatic and less aggressive MCF7 cells tend to acquire pro-metastatic characteristics. Conversely, post-PBI descendants of highly metastatic and more aggressive MDA-MB-231 cells exhibit a marked reduction in these traits under similar conditions. Our findings emphasize the limitations of using 2D environments such as rigid plastic culture dishes in distinguishing highly deformable cancer cells with increased metastatic potential and tumor repopulation capacity. This becomes particularly evident with parental MDA-MB-231 and MCF7RP cells acquiring "softness" when cultured in soft conditions such as a 90 Pa fibrin layer, a trait that correlates with the larger tumor sizes observed *in vivo*. A limitation of this study is the use of only two BC cell lines, representing just two of the four recognized molecular subtypes. However, the observed association between their distinct molecular phenotypes and differential responses to PBI suggests a potential avenue for developing more personalized treatment strategies tailored to patients with specific molecular profiles and tumor stiffness. Further studies are needed to examine the response of additional BC molecular subtypes to PBI, either alone or in combination with chemotherapy. Potential treatment enhancements could include recently suggested STAT3-targeting inhibitors [109] or natural compounds such as ellagic acid [110], which may improve antitumor efficacy while minimizing adverse effects. Overall our research demonstrates that high-LET proton irradiation significantly alters the tumorigenic potential of BC cell lines *in vivo*, particularly when compared to their syngeneic parental counterparts. Results from our clonogenic (*in vitro*) and CAM (*in vivo*) assays not only validate the superior effectiveness of proton beams but also endorse their targeted application in certain cancer therapies.

Availability of Data and Materials

All data reported in this paper will be shared by the lead contact upon request.

Author Contributions

MP—original draft preparation, project management, methodology and conceptualization. RM, YW, WX, PM, VN, EK, ZN, DK—formal analysis, research, visualization. VS—irradiation. SL, and MP—funding acquisition. MP—writing. AO, SL—writing-review and editing and conceptualization. All authors contributed to editorial changes in the manuscript. All authors read and approved the final manuscript. All authors have participated sufficiently in the work and agreed to be accountable for all aspects of the work.

Ethics Approval and Consent to Participate

All animal experiments in this study were conducted in strict compliance with the guidelines and regulations of the Institutional Animal Care and Use Committee (IACUC). Chicken embryos are not classified as living animals until 17 days of incubation, and our experiments with CAM were completed by embryonic day 16 (E16), which were exempt from IACUC regulation. Additionally, in adherence to the Russian Animal Experiment and Welfare Guidelines, ethical approval was not required.

Acknowledgment

The authors wish to express their sincere appreciation to the "Proton radiation complex" group at the A. Tsyb Medical Radiological Research Centre (MRRC, Obninsk, Russia) for providing the irradiation experiments essential to this study.

Funding

This research was funded by the Ministry of Science and Higher Education of the Russian Federation (State Task) 075-03-2024-117/113, Project No. FSMG-2024-0045.

Conflict of Interest

The authors declare no conflict of interest.

Supplementary Material

Supplementary material associated with this article can be found, in the online version, at https://doi.org/10.31083/FBL36415.

References

[1] Watkins EJ. Overview of breast cancer. Journal of the American Academy of Physician Assistants. 2019; 32: 13–17. https://doi.org/10.1097/01.JAA.0000580524.95733.3d.

[2] Loibl S, André F, Bachelot T, Barrios CH, Bergh J, Burstein HJ, *et al*. Early breast cancer: ESMO Clinical Practice Guideline for diagnosis, treatment and follow-up. Annals of Oncology. 2024; 35: 159–182. https://doi.org/10.1016/j.annonc.2023.11.016.

[3] Gennari A, André F, Barrios CH, Cortés J, de Azambuja E, DeMichele A, *et al*. ESMO Clinical Practice Guideline for the diagnosis, staging and treatment of patients with metastatic breast cancer. Annals of Oncology. 2021; 32: 1475–1495. https://doi.org/10.1016/j.annonc.2021.09.019.

[4] Musielak M, Suchorska WM, Fundowicz M, Milecki P, Malicki J. Future Perspectives of Proton Therapy in Minimizing the Toxicity of Breast Cancer Radiotherapy. Journal of Personalized Medicine. 2021; 11: 410. https://doi.org/10.3390/jpm11050410.

[5] Nikitaki Z, Velalopoulou A, Zanni V, Tremi I, Havaki S, Kokkoris M, *et al*. Key biological mechanisms involved in high-LET radiation therapies with a focus on DNA damage and repair. Expert Reviews in Molecular Medicine. 2022; 24: e15. https://doi.org/10.1017/erm.2022.6.

[6] Mutter RW, Choi JI, Jimenez RB, Kirova YM, Fagundes M, Haffty BG, *et al*. Proton Therapy for Breast Cancer: A Consensus Statement From the Particle Therapy Cooperative Group Breast Cancer Subcommittee. International Journal of Radiation Oncology, Biology, Physics. 2021; 111: 337–359. https://doi.org/10.1016/j.ijrobp.2021.05.110.

[7] Holt F, Probert J, Darby SC, Haviland JS, Coles CE, Kirby AM, *et al*. Proton Beam Therapy for Early Breast Cancer: A Systematic Review and Meta-analysis of Clinical Outcomes. International Journal of Radiation Oncology, Biology, Physics. 2023; 117: 869–882. https://doi.org/10.1016/j.ijrobp.2023.02.023.

[8] Wu XY, Chen M, Cao L, Li M, Chen JY. Proton Therapy in Breast Cancer: A Review of Potential Approaches for Patient Selection. Technology in Cancer Research & Treatment. 2024; 23: 15330338241234788. https://doi.org/10.1177/15330338241234788.

[9] Mohammed AA. The clinical behavior of different molecular subtypes of breast cancer. Cancer Treatment and Research Communications. 2021; 29: 100469. https://doi.org/10.1016/j.ctarc.2021.100469.

[10] Suhani, Parshad R, Kazi M, Seenu V, Mathur S, Dattagupta S, *et al*. Triple-negative breast cancers: Are they always different from nontriple-negative breast cancers? An experience from a tertiary center in India. Indian Journal of Cancer. 2017; 54: 658–663. https://doi.org/10.4103/ijc.IJC_348_17.

[11] Wambersie A, Hendry J, Gueulette J, Gahbauer R, Pötter R, Grégoire V. Radiobiological rationale and patient selection for high-LET radiation in cancer therapy. Radiotherapy and Oncology: Journal of the European Society for Therapeutic Radiology and Oncology. 2004; 73: S1–S14. https://doi.org/10.1016/s0167-8140(04)80004-5.

[12] Bravatà V, Minafra L, Cammarata FP, Pisciotta P, Lamia D, Marchese V, *et al*. Gene expression profiling of breast cancer cell lines treated with proton and electron radiations. The British Journal of Radiology. 2018; 91: 20170934. https://doi.org/10.1259/bjr.20170934.

[13] Cammarata FP, Forte GI, Broggi G, Bravatà V, Minafra L, Pisciotta P, *et al*. Molecular Investigation on a Triple Negative Breast Cancer Xenograft Model Exposed to Proton Beams. International Journal of Molecular Sciences. 2020; 21: 6337. https://doi.org/10.3390/ijms21176337.

[14] Ding LH, Park S, Peyton M, Girard L, Xie Y, Minna JD, *et al*. Distinct transcriptome profiles identified in normal human bronchial epithelial cells after exposure to γ-rays and different elemental particles of high Z and energy. BMC Genomics. 2013; 14: 372. https://doi.org/10.1186/1471-2164-14-372.

[15] Macaeva E, Tabury K, Michaux A, Janssen A, Averbeck N, Moreels M, *et al*. High-LET Carbon and Iron Ions Elicit a Prolonged and Amplified p53 Signaling and Inflammatory Response Compared to low-LET X-Rays in Human Peripheral Blood Mononuclear Cells. Frontiers in Oncology. 2021; 11: 768493. https://doi.org/10.3389/fonc.2021.768493.

[16] Michalettou TD, Michalopoulos I, Costes SV, Hellweg CE, Hada M, Georgakilas AG. A Meta-Analysis of the Effects of High-LET Ionizing Radiations in Human Gene Expression. Life. 2021; 11: 115. https://doi.org/10.3390/life11020115.

[17] Sertorio M, Nowrouzi A, Akbarpour M, Chetal K, Salomonis N, Brons S, *et al*. Differential transcriptome response to proton versus X-ray radiation reveals novel candidate targets for combinatorial PT therapy in lymphoma. Radiotherapy and Oncology. 2021; 155: 293–303. https://doi.org/10.1016/j.radonc.2020.10.024.

[18] Flint DB, Ruff CE, Bright SJ, Yepes P, Wang Q, Manandhar M, *et al*. An empirical model of proton RBE based on the linear correlation between x-ray and proton radiosensitivity. Medical Physics. 2022; 49: 6221–6236. https://doi.org/10.1002/mp.15850.

[19] Takahashi A, Kubo M, Ma H, Nakagawa A, Yoshida Y, Isono M, *et al*. Nonhomologous end-joining repair plays a more important role than homologous recombination repair in defining radiosensitivity after exposure to high-LET radiation. Radiation Research. 2014; 182: 338–344. https://doi.org/10.1667/RR13782.1.

[20] Li X, Heyer WD. Homologous recombination in DNA repair and DNA damage tolerance. Cell Research. 2008; 18: 99–113. https://doi.org/10.1038/cr.2008.1.

[21] Stinson BM, Loparo JJ. Repair of DNA Double-Strand Breaks by the Nonhomologous End Joining Pathway. Annual Review of Biochemistry. 2021; 90: 137–164. https://doi.org/10.1146/annurev-biochem-080320-110356.

[22] Mirza-Aghazadeh-Attari M, Mohammadzadeh A, Yousefi B, Mihanfar A, Karimian A, Majidinia M. 53BP1: A key player of DNA damage response with critical functions in cancer. DNA Repair. 2019; 73: 110–119. https://doi.org/10.1016/j.dnarep.2018.11.008.

[23] Bouwman P, Aly A, Escandell JM, Pieterse M, Bartkova J, van der Gulden H, *et al*. 53BP1 loss rescues BRCA1 deficiency and is associated with triple-negative and BRCA-mutated breast cancers. Nature Structural & Molecular Biology. 2010; 17: 688–695. https://doi.org/10.1038/nsmb.1831.

[24] Zimmermann M, de Lange T. 53BP1: pro choice in DNA repair. Trends in Cell Biology. 2014; 24: 108–117. https://doi.org/10.1016/j.tcb.2013.09.003.

[25] Escribano-Díaz C, Orthwein A, Fradet-Turcotte A, Xing M, Young JTF, Tkáč J, *et al*. A cell cycle-dependent regulatory circuit composed of 53BP1-RIF1 and BRCA1-CtIP controls DNA repair pathway choice. Molecular Cell. 2013; 49: 872–883. https://doi.org/10.1016/j.molcel.2013.01.001.

[26] Mirman Z, de Lange T. 53BP1: a DSB escort. Genes & Development. 2020; 34: 7–23. https://doi.org/10.1101/gad.333237.119.

[27] Lottersberger F, Karssemeijer RA, Dimitrova N, de Lange T. 53BP1 and the LINC Complex Promote Microtubule-Dependent DSB Mobility and DNA Repair. Cell. 2015; 163: 880–893. https://doi.org/10.1016/j.cell.2015.09.057.

[28] Lee KJ, Saha J, Sun J, Fattah KR, Wang SC, Jakob B, *et al*. Phosphorylation of Ku dictates DNA double-strand break (DSB) repair pathway choice in S phase. Nucleic Acids Research. 2016; 44: 1732–1745. https://doi.org/10.1093/nar/gkv1499.

[29] Friedl P, Wolf K. Tumour-cell invasion and migration: diversity and escape mechanisms. Nature Reviews. Cancer. 2003; 3: 362–374. https://doi.org/10.1038/nrc1075.

[30] Fanfone D, Wu Z, Mammi J, Berthenet K, Neves D, Weber K, *et al*. Confined migration promotes cancer metastasis through resistance to anoikis and increased invasiveness. eLife. 2022; 11: e73150. https://doi.org/10.7554/eLife.73150.

[31] Fujita M, Yamada S, Imai T. Irradiation induces diverse changes in invasive potential in cancer cell lines. Seminars in Cancer Biology. 2015; 35: 45–52. https://doi.org/10.1016/j.semcancer.2015.09.003.

[32] Jasińska-Konior K, Pochylczuk K, Czajka E, Michalik M, Romanowska-Dixon B, Swakoń J, *et al*. Proton beam irradiation inhibits the migration of melanoma cells. PLoS ONE. 2017; 12: e0186002. https://doi.org/10.1371/journal.pone.0186002.

[33] Onea M, Bacalum M, Radulescu AL, Raileanu M, Craciun L, Esanu TR, *et al*. Electrochemical evaluation of proton beam radiation effect on the B16 cell culture. Scientific Reports. 2022; 12: 2261. https://doi.org/10.1038/s41598-022-06277-6.

[34] Mahmoud A, Casciati A, Bakar ZA, Hamzah H, Ahmad TAT, Noor MHM. The Detection of DNA Damage Response in MCF7 and MDA-MB-231 Breast Cancer Cell Lines after X-ray Exposure. Genome Integrity. 2023; 14: e20220001. https://doi.org/10.14293/genint.14.1.001.

[35] Musolino SV. Absorbed dose determination in external beam radiotherapy: an international code of practice for dosimetry based on standards of absorbed dose to water; technical reports series No. 398. Health Physics. 2001; 81: 592–593. https://doi.org/10.1097/00004032-200111000-00017.

[36] Zhang J, Ha W, Chang Y, Ge Y, Wei X, Tan Y, *et al*. Tumorigenic cell selection and substrate rigidity manipulation using 2D and 3D extracellular matrices. STAR Protocols. 2022; 3: 101577. https://doi.org/10.1016/j.xpro.2022.101577.

[37] Merkher Y, Kontareva E, Bogdan E, Achkasov K, Maximova K, Grolman JM, *et al*. Encapsulation and adhesion of nanoparticles as a potential biomarker for TNBC cells metastatic propensity. Scientific Reports. 2023; 13: 12289. https://doi.org/10.1038/s41598-023-33540-1.

[38] Rheinlaender J, Schäffer TE. Mapping the mechanical stiffness of live cells with the scanning ion conductance microscope. Soft Matter. 2013; 9: 3230–3236. https://doi.org/10.1039/C2SM27412D.

[39] Sarogni P, Mapanao AK, Marchetti S, Kusmic C, Voliani V. A Standard Protocol for the Production and Bioevaluation of Ethical *In Vivo* Models of HPV-Negative Head and Neck Squamous Cell Carcinoma. ACS Pharmacology & Translational Science. 2021; 4: 1227–1234. https://doi.org/10.1021/acsptsci.1c00083.

[40] Ribatti D, Annese T. Chick embryo in experimental embryology and more. Pathology, Research and Practice. 2023; 245: 154478. https://doi.org/10.1016/j.prp.2023.154478.

[41] Abolfath R, Peeler CR, Newpower M, Bronk L, Grosshans D, Mohan R. A model for relative biological effectiveness of therapeutic proton beams based on a global fit of cell survival data. Scientific Reports. 2017; 7: 8340. https://doi.org/10.1038/s41598-017-08622-6.

[42] Blackford AN, Jackson SP. ATM, ATR, and DNA-PK: The Trinity at the Heart of the DNA Damage Response. Molecular Cell. 2017; 66: 801–817. https://doi.org/10.1016/j.molcel.2017.05.015.

[43] Suzuki M, Boothman DA. Stress-induced premature senescence (SIPS)–influence of SIPS on radiotherapy. Journal of Radiation Research. 2008; 49: 105–112. https://doi.org/10.1269/jrr.07081.

[44] Kim BC, Han NK, Byun HO, Kim SS, Ahn EK, Chu IS, *et al*. Time-dependently expressed markers and the characterization for premature senescence induced by ionizing radiation in MCF7. Oncology Reports. 2010; 24: 395–403. https://doi.org/10.3892/or_00000872.

[45] Valieva Y, Ivanova E, Fayzullin A, Kurkov A, Igrunkova A. Senescence-Associated β-Galactosidase Detection in Pathology. Diagnostics. 2022; 12: 2309. https://doi.org/10.3390/diagnostics12102309.

[46] Mlynarczuk-Bialy I, Dziuba I, Sarnecka A, Platos E, Kowalczyk M, Pels KK, *et al*. Entosis: From Cell Biology to Clinical Cancer Pathology. Cancers. 2020; 12: 2481. https://doi.org/10.3390/cancers12092481.

[47] Solovieva M, Shatalin Y, Odinokova I, Krestinina O, Baburina Y, Mishukov A, *et al*. Disulfiram oxy-derivatives induce entosis or paraptosis-like death in breast cancer MCF-7 cells depending on the duration of treatment. Biochimica et Biophysica Acta. General Subjects. 2022; 1866: 130184. https://doi.org/10.1016/j.bbagen.2022.130184.

[48] Clarke R. Cannibalism, cell survival, and endocrine resistance in breast cancer. Breast Cancer Research. 2011; 13: 311. https://doi.org/10.1186/bcr2870.

[49] Haupt S, Keam SP, Haupt Y. Cannibalism in Breast Cancer: The Dangers of Overeating. Trends in Cancer. 2019; 5: 761–762. https://doi.org/10.1016/j.trecan.2019.10.008.

[50] Makale M. Cellular mechanobiology and cancer metastasis. Birth Defects Research. Part C, Embryo Today: Reviews. 2007; 81: 329–343. https://doi.org/10.1002/bdrc.20110.

[51] Yang J, Antin P, Berx G, Blanpain C, Brabletz T, Bronner M, *et al*. Guidelines and definitions for research on epithelial-mesenchymal transition. Nature Reviews [published correction in Nature Reviews. Molecular Cell Biology. 2021; 22: 834. https://doi.org/10.1038/s41580-021-00428-9]. Molecular Cell Biology. 2020; 21: 341–352. https://doi.org/10.1038/s41580-020-0237-9.

[52] Wang Y, Shi J, Chai K, Ying X, Zhou BP. The Role of Snail in EMT and Tumorigenesis. Current Cancer Drug Targets. 2013; 13: 963–972. https://doi.org/10.2174/15680096113136660102.

[53] Liu J, Tan Y, Zhang H, Zhang Y, Xu P, Chen J, *et al*. Soft fibrin gels promote selection and growth of tumorigenic cells [published correction in Nature Materials. 2021; 20: 905. https://doi.org/10.1038/s41563-021-01032-0]. Nature Materials. 2012; 11: 734–741. https://doi.org/10.1038/nmat3361.

[54] Safaei S, Sajed R, Shariftabrizi A, Dorafshan S, Saeednejad Zanjani L, Dehghan Manshadi M, *et al*. Tumor matrix stiffness provides fertile soil for cancer stem cells. Cancer Cell International. 2023; 23: 143. https://doi.org/10.1186/s12935-023-02992-w.

[55] Chang J, Saraswathibhatla A, Song Z, Varma S, Sanchez C, Alyafei NHK, *et al*. Cell volume expansion and local contractility drive collective invasion of the basement membrane in breast cancer. Nature Materials. 2024; 23: 711–722. https://doi.org/10.1038/s41563-023-01716-9.

[56] Hu S, Chen J, Fabry B, Numaguchi Y, Gouldstone A, Ingber DE, *et al*. Intracellular stress tomography reveals stress focusing and structural anisotropy in cytoskeleton of living cells. Ameri-

can Journal of Physiology. Cell Physiology. 2003; 285: C1082–C1090. https://doi.org/10.1152/ajpcell.00159.2003.
[57] Fischer T, Hayn A, Mierke CT. Effect of Nuclear Stiffness on Cell Mechanics and Migration of Human Breast Cancer Cells. Front Cell Dev Biol. 2020; 8: 393. https://doi.org/10.3389/fcell.2020.00393.
[58] Aermes C, Hayn A, Fischer T, Mierke CT. Cell mechanical properties of human breast carcinoma cells depend on temperature. Sci Rep. 2021; 11: 10771. https://doi.org/10.1038/s41598-021-90173-y.
[59] Lokman NA, Elder ASF, Ricciardelli C, Oehler MK. Chick chorioallantoic membrane (CAM) assay as an in vivo model to study the effect of newly identified molecules on ovarian cancer invasion and metastasis. International Journal of Molecular Sciences. 2012; 13: 9959–9970. https://doi.org/10.3390/ijms13089959.
[60] Ribatti D. The chick embryo chorioallantoic membrane as a model for tumor biology. Experimental Cell Research. 2014; 328: 314–324. https://doi.org/10.1016/j.yexcr.2014.06.010.
[61] Kleibeuker EA, Ten Hooven MA, Castricum KC, Honeywell R, Griffioen AW, Verheul HM, *et al*. Optimal treatment scheduling of ionizing radiation and sunitinib improves the antitumor activity and allows dose reduction. Cancer Medicine. 2015; 4: 1003–1015. https://doi.org/10.1002/cam4.441.
[62] Sung H, Ferlay J, Siegel RL, Laversanne M, Soerjomataram I, Jemal A, *et al*. Global Cancer Statistics 2020: GLOBOCAN Estimates of Incidence and Mortality Worldwide for 36 Cancers in 185 Countries. CA: a Cancer Journal for Clinicians. 2021; 71: 209–249. https://doi.org/10.3322/caac.21660.
[63] Cannan WJ, Pederson DS. Mechanisms and Consequences of Double-Strand DNA Break Formation in Chromatin. Journal of Cellular Physiology. 2016; 231: 3–14. https://doi.org/10.1002/jcp.25048.
[64] Nickoloff JA, Sharma N, Taylor L. Clustered DNA Double-Strand Breaks: Biological Effects and Relevance to Cancer Radiotherapy. Genes. 2020; 11: 99. https://doi.org/10.3390/genes11010099.
[65] Pustovalova M, Alhaddad L, Smetanina N, Chigasova A, Blokhina T, Chuprov-Netochin R, *et al*. The p53-53BP1-Related Survival of A549 and H1299 Human Lung Cancer Cells after Multifractionated Radiotherapy Demonstrated Different Response to Additional Acute X-ray Exposure. International Journal of Molecular Sciences. 2020; 21: 3342. https://doi.org/10.3390/ijms21093342.
[66] Alhaddad L, Pustovalova M, Blokhina T, Chuprov-Netochin R, Osipov AN, Leonov S. IR-Surviving NSCLC Cells Exhibit Different Patterns of Molecular and Cellular Reactions Relating to the Multifraction Irradiation Regimen and p53-Family Proteins Expression. Cancers. 2021; 13: 2669. https://doi.org/10.3390/cancers13112669.
[67] Pustovalova M, Malakhov P, Guryanova A, Sorokin M, Suntsova M, Buzdin A, *et al*. Transcriptome-Based Traits of Radioresistant Sublines of Non-Small Cell Lung Cancer Cells. International Journal of Molecular Sciences. 2023; 24: 3042. https://doi.org/10.3390/ijms24033042.
[68] Pustovalova MV, Guryanova AA, Sorokin MI, Suntsova MV, Buzdin AA, Alhaddad L, *et al*. Transcriptomic Analysis of DNA Repair Pathways in Human Non-Small Cell Lung Cancer Cells Surviving Multifraction X-Ray Irradiation. Bulletin of Experimental Biology and Medicine. 2022; 173: 454–458. https://doi.org/10.1007/s10517-022-05586-0.
[69] Penninckx S, Pariset E, Cekanaviciute E, Costes SV. Quantification of radiation-induced DNA double strand break repair foci to evaluate and predict biological responses to ionizing radiation. NAR Cancer. 2021; 3: zcab046. https://doi.org/10.1093/narcan/zcab046.
[70] Bridges AE, Ramachandran S, Pathania R, Parwal U, Lester A, Rajpurohit P, *et al*. *RAD51AP1* Deficiency Reduces Tumor Growth by Targeting Stem Cell Self-Renewal. Cancer Research. 2020; 80: 3855–3866. https://doi.org/10.1158/0008-5472.CAN-19-3713.
[71] Sagkrioti E, Biz GM, Takan I, Asfa S, Nikitaki Z, Zanni V, *et al*. Radiation Type- and Dose-Specific Transcriptional Responses across Healthy and Diseased Mammalian Tissues. Antioxidants. 2022; 11: 2286. https://doi.org/10.3390/antiox11112286.
[72] He S, Sharpless NE. Senescence in Health and Disease. Cell. 2017; 169: 1000–1011. https://doi.org/10.1016/j.cell.2017.05.015.
[73] Pustovalova M, Blokhina T, Alhaddad L, Chigasova A, Chuprov-Netochin R, Veviorskiy A, *et al*. CD44+ and CD133+ Non-Small Cell Lung Cancer Cells Exhibit DNA Damage Response Pathways and Dormant Polyploid Giant Cancer Cell Enrichment Relating to Their p53 Status. International Journal of Molecular Sciences. 2022; 23: 4922. https://doi.org/10.3390/ijms23094922.
[74] Alhaddad L, Chuprov-Netochin R, Pustovalova M, Osipov AN, Leonov S. Polyploid/Multinucleated Giant and Slow-Cycling Cancer Cell Enrichment in Response to X-ray Irradiation of Human Glioblastoma Multiforme Cells Differing in Radioresistance and TP53/PTEN Status. International Journal of Molecular Sciences. 2023; 24: 1228. https://doi.org/10.3390/ijms24021228.
[75] Alhaddad L, Nofal Z, Pustovalova M, Osipov AN, Leonov S. Long-Term Cultured Human Glioblastoma Multiforme Cells Demonstrate Increased Radiosensitivity and Senescence-Associated Secretory Phenotype in Response to Irradiation. International Journal of Molecular Sciences. 2023; 24: 2002. https://doi.org/10.3390/ijms24032002.
[76] Lagadec C, Vlashi E, Della Donna L, Meng Y, Dekmezian C, Kim K, *et al*. Survival and self-renewing capacity of breast cancer initiating cells during fractionated radiation treatment. Breast Cancer Research. 2010; 12: R13. https://doi.org/10.1186/bcr2479.
[77] Overholtzer M, Mailleux AA, Mouneimne G, Normand G, Schnitt SJ, King RW, *et al*. A nonapoptotic cell death process, entosis, that occurs by cell-in-cell invasion. Cell. 2007; 131: 966–979. https://doi.org/10.1016/j.cell.2007.10.040.
[78] Bauer MF, Hildebrand LS, Rosahl MC, Erber R, Schnellhardt S, Büttner-Herold M, *et al*. Cell-In-Cell Structures in Early Breast Cancer Are Prognostically Valuable. Cells. 2022; 12: 81. https://doi.org/10.3390/cells12010081.
[79] Schwegler M, Wirsing AM, Schenker HM, Ott L, Ries JM, Büttner-Herold M, *et al*. Prognostic Value of Homotypic Cell Internalization by Nonprofessional Phagocytic Cancer Cells. BioMed Research International. 2015; 2015: 359392. https://doi.org/10.1155/2015/359392.
[80] Zhang X, Niu Z, Qin H, Fan J, Wang M, Zhang B, *et al*. Subtype-Based Prognostic Analysis of Cell-in-Cell Structures in Early Breast Cancer. Frontiers in Oncology. 2019; 9: 895. https://doi.org/10.3389/fonc.2019.00895.
[81] Pustovalova MV, Yashkina EI, Alhaddad L, Osipov AN, Chen Y, Leonov SV. Phenotypic Characteristics of Dormant Human Non-Small Cell Lung Cancer Cells Surviving Multifraction X-Ray Irradiation. Bulletin of Experimental Biology and Medicine. 2022; 174: 76–80. https://doi.org/10.1007/s10517-022-05652-7.
[82] Schaeffer D, Somarelli JA, Hanna G, Palmer GM, Garcia-Blanco MA. Cellular migration and invasion uncoupled: increased migration is not an inexorable consequence of epithelial-to-mesenchymal transition. Molecular and Cellular Biology. 2014; 34: 3486–3499. https://doi.org/10.1128/MCB.00694-14.
[83] Ladoux B, Mège RM. Mechanobiology of collective cell be-

haviours. Nature Reviews. Molecular Cell Biology. 2017; 18: 743–757. https://doi.org/10.1038/nrm.2017.98.

[84] Guck J, Schinkinger S, Lincoln B, Wottawah F, Ebert S, Romeyke M, *et al*. Optical deformability as an inherent cell marker for testing malignant transformation and metastatic competence. Biophysical Journal. 2005; 88: 3689–3698. https://doi.org/10.1529/biophysj.104.045476.

[85] Lv J, Liu Y, Huang B. Mechanical softness: a true stemness feature for cancer cells. Molecular & Cellular Oncology. 2021; 8: 1882285. https://doi.org/10.1080/23723556.2021.1882285.

[86] Cross SE, Jin YS, Rao J, Gimzewski JK. Nanomechanical analysis of cells from cancer patients. Nature Nanotechnology. 2007; 2: 780–783. https://doi.org/10.1038/nnano.2007.388.

[87] Sun Q, Luo T, Ren Y, Florey O, Shirasawa S, Sasazuki T, *et al*. Competition between human cells by entosis. Cell Research. 2014; 24: 1299–1310. https://doi.org/10.1038/cr.2014.138.

[88] Ge H, Tian M, Pei Q, Tan F, Pei H. Extracellular Matrix Stiffness: New Areas Affecting Cell Metabolism. Frontiers in Oncology. 2021; 11: 631991. https://doi.org/10.3389/fonc.2021.631991.

[89] Vahala D, Amos SE, Sacchi M, Soliman BG, Hepburn MS, Mowla A, *et al*. 3D Volumetric Mechanosensation of MCF7 Breast Cancer Spheroids in a Linear Stiffness Gradient GelAGE. Advanced Healthcare Materials. 2023; 12: e2301506. https://doi.org/10.1002/adhm.202301506.

[90] Plodinec M, Loparic M, Monnier CA, Obermann EC, Zanetti-Dallenbach R, Oertle P, *et al*. The nanomechanical signature of breast cancer. Nature Nanotechnology. 2012; 7: 757–765. https://doi.org/10.1038/nnano.2012.167.

[91] Coffin ST, Gaudette GR. Aprotinin extends mechanical integrity time of cell-seeded fibrin sutures. Journal of Biomedical Materials Research. Part A. 2016; 104: 2271–2279. https://doi.org/10.1002/jbm.a.35754.

[92] Wei F, Xu X, Zhang C, Liao Y, Ji B, Wang N. Stress fiber anisotropy contributes to force-mode dependent chromatin stretching and gene upregulation in living cells. Nature Communications. 2020; 11: 4902. https://doi.org/10.1038/s41467-020-18584-5.

[93] Wang N, Butler JP, Ingber DE. Mechanotransduction across the cell surface and through the cytoskeleton. Science. 1993; 260: 1124–1127. https://doi.org/10.1126/science.7684161.

[94] Hu S, Eberhard L, Chen J, Love JC, Butler JP, Fredberg JJ, *et al*. Mechanical anisotropy of adherent cells probed by a three-dimensional magnetic twisting device. American Journal of Physiology. Cell Physiology. 2004; 287: C1184–C1191. https://doi.org/10.1152/ajpcell.00224.2004.

[95] Gil-Redondo JC, Weber A, Zbiral B, Vivanco MD, Toca-Herrera JL. Substrate stiffness modulates the viscoelastic properties of MCF-7 cells. Journal of the Mechanical Behavior of Biomedical Materials. 2022; 125: 104979. https://doi.org/10.1016/j.jmbbm.2021.104979.

[96] Amiri S, Muresan C, Shang X, Huet-Calderwood C, Schwartz MA, Calderwood DA, *et al*. Intracellular tension sensor reveals mechanical anisotropy of the actin cytoskeleton. Nature Communications. 2023; 14: 8011. https://doi.org/10.1038/s41467-023-43612-5.

[97] Pizon M, Schott D, Pachmann U, Schobert R, Pizon M, Wozniak M, *et al*. Chick Chorioallantoic Membrane (CAM) Assays as a Model of Patient-Derived Xenografts from Circulating Cancer Stem Cells (cCSCs) in Breast Cancer Patients. Cancers. 2022; 14: 1476. https://doi.org/10.3390/cancers14061476.

[98] Comșa Ș, Popescu R, Avram Ș, Ceaușu RA, Cîmpean AM, Raica M. Bevacizumab Modulation of the Interaction Between the MCF-7 Cell Line and the Chick Embryo Chorioallantoic Membrane. In Vivo. 2017; 31: 199–203. https://doi.org/10.21873/invivo.11045.

[99] Ranjan RA, Muenzner JK, Kunze P, Geppert CI, Ruebner M, Huebner H, *et al*. The Chorioallantoic Membrane Xenograft Assay as a Reliable Model for Investigating the Biology of Breast Cancer. Cancers. 2023; 15: 1704. https://doi.org/10.3390/cancers15061704.

[100] ComȘa Ș, CeauȘu AR, Popescu R, SÂrb S, CÎmpean AM, Raica M. The MSC-MCF-7 Duet Playing Tumor Vasculogenesis and Angiogenesis onto the Chick Embryo Chorioallantoic Membrane. In Vivo. 2020; 34: 3315–3325. https://doi.org/10.21873/invivo.12170.

[101] Comsa S, Ceausu AR, Popescu R, Cimpean AM, Sarb S, Raica M. Patterns of Tumor Vasculogenesis on a Chick Embryo Chorioallantoic Membrane *In Vivo* Model of Breast Cancer. Anticancer Research. 2022; 42: 877–883. https://doi.org/10.21873/anticanres.15545.

[102] La Verde G, Artiola V, Panzetta V, Pugliese M, Netti PA, Fusco S. Cytoskeleton Response to Ionizing Radiation: A Brief Review on Adhesion and Migration Effects. Biomedicines. 2021; 9: 1102. https://doi.org/10.3390/biomedicines9091102.

[103] Sun Z, Guo SS, Fässler R. Integrin-mediated mechanotransduction. The Journal of Cell Biology. 2016; 215: 445–456. https://doi.org/10.1083/jcb.201609037.

[104] Shapovalov G, Ritaine A, Skryma R, Prevarskaya N. Role of TRP ion channels in cancer and tumorigenesis. Seminars in Immunopathology. 2016; 38: 357–369. https://doi.org/10.1007/s00281-015-0525-1.

[105] Low BC, Pan CQ, Shivashankar GV, Bershadsky A, Sudol M, Sheetz M. YAP/TAZ as mechanosensors and mechanotransducers in regulating organ size and tumor growth. FEBS Letters. 2014; 588: 2663–2670. https://doi.org/10.1016/j.febslet.2014.04.012.

[106] Zheng Q, Liu Y, Zhou HJ, Du YT, Zhang BP, Zhang J, *et al*. X-ray radiation promotes the metastatic potential of tongue squamous cell carcinoma cells via modulation of biomechanical and cytoskeletal properties. Human & Experimental Toxicology. 2015; 34: 894–903. https://doi.org/10.1177/0960327114561664.

[107] Musielak M, Graczyk K, Liszka M, Christou A, Rosochowicz MA, Lach MS, *et al*. Impact of Proton Irradiation Depending on Breast Cancer Subtype in Patient-Derived Cell Lines. International Journal of Molecular Sciences. 2024; 25: 10494. https://doi.org/10.3390/ijms251910494.

[108] Bravatà V, Cammarata FP, Minafra L, Pisciotta P, Scazzone C, Manti L, *et al*. Proton-irradiated breast cells: molecular points of view. Journal of Radiation Research. 2019; 60: 451–465. https://doi.org/10.1093/jrr/rrz032.

[109] Zamanian MY, Golmohammadi M, Alalak A, Kamiab Z, Obaid R, Ramírez-Coronel AA, *et al*. STAT3 Signaling Axis and Tamoxifen in Breast Cancer: A Promising Target for Treatment Resistance. Anti-Cancer Agents in Medicinal Chemistry. 2023; 23: 1819–1828. https://doi.org/10.2174/1871520623666230713101119.

[110] Golmohammadi M, Zamanian MY, Jalal SM, Noraldeen SAM, Ramírez-Coronel AA, Oudaha KH, *et al*. A comprehensive review on Ellagic acid in breast cancer treatment: From cellular effects to molecular mechanisms of action. Food Science & Nutrition. 2023; 11: 7458–7468. https://doi.org/10.1002/fsn3.3699.